CONF-8603116--1

CONF-8603116--1

DE86 010528

# ANALYSIS OF THE FELIX EXPERIMENTS WITH CANTILEVERED BEAMS AND HOLLOW CYLINDERS*

L. R. Turner, T. Q. Hua, and S. Y. Lee



Argonne National Laboratory
9700 South Cass Avenue
Argonne, Illinois 60439

Paper presented at the

Fourth Eddy Current Seminar
Rutherford Appleton Laboratory

March 24-26, 1986



*Work supported by the U.S. Department of Energy/Office of Fusion Energy.

# ANALYSIS OF THE FELIX EXPERIMENTS WITH CANTILEVERED BEAMS AND HOLLOW CYLINDERS*

L. R. Turner, T. Q. Hua†, S.-Y. Lee‡
Argonne National Laboratory
Argonne, Illinois 60439 USA

## Abstract

Experiments have been performed with the FELIX facility at Argonne National Laboratory to study the coupling between eddy currents and deflections and to provide data for validating eddy current computer programs. Experiments with cantilevered beams in crossed steady and decaying magnetic fields verify that coupling effects act to alleviate the large currents, deflections, and stresses predicted by uncoupled analyses. Measurements of magnetic fields induced in conducting hollow cylinders are analyzed by exponential fitting and by transfer functions. Spatial variation in the parameters of the exponential fit and in those of the one- and two-pole transfer functions suggests that several eddy current modes are acting in the cylinder test pieces.

---

* Work supported by the U.S. Department of Energy.

† Magnetic Fusion Energy Technology Fellow at Argonne National Laboratory

‡ also with the Department of Electrical Engineering, Korea Advanced Institute of Science & Technology

## 1. Introduction

Existing eddy current codes, and new ones as they are developed, must be validated against experimental data representing geometry and operation similar to those of a fusion reactor. Consequently, the early experiments with the FELIX[1,2] facility have been devoted to obtaining data which can be used to validate eddy current computer codes.

The FELIX facility at Argonne National Laboratory (ANL) includes:

1) A solenoid magnet producing fields up to 1 T.

2) A dipole magnet surrounding the solenoid and producing fields up to 0.5 T perpendicular to the solenoid field.

3) A switching circuit capable of discharging the dipole field with a time constant as low as 5 ms.

4) A cylindrical experimental volume within the fields of the two magnets of dimensions 1.2 m axially by 0.9 m diameter, and with convenient access.

5) Non-conducting test-piece supports.

6) Instrumentation suitable for measuring currents, magnetic fields, angular displacements, temperatures, and stresses.

7) Computerized data acquisition with provision for recording values at 2048 times on as many as 30 data channels.

Five major series of experiments have been conducted:

1) Experiments on the coupling between eddy currents and angular displacements of loops and plates in crossed constant and changing fields as a model of tokamak limiters. These experiments were carried out by a team

of investigators from Princeton Plasma Physics Laboratory (PPPL) and ANL, and verified that coupling effects lower the eddy currents and displacements and thus decrease the design constraints on limiters.

2) Experiments on the coupling between eddy currents and angular displacements in cantilevered beams. These experiments carried out for a PhD dissertaion from the University of Washington, Seattle, extended the coupling results to a more realistic model of tokamak limiters.

3) Experiments measuring eddy current effects in hollow cylinders. These experiments explored the limitations of using 2-D codes to model 3-D geometries.

4) Experiments measuring eddy current effects in flat plates. These experiments were conducted to validate 2-D and 3-D eddy current computer codes.

5) Experiments measuring eddy currents and field patterns around conducting bricks. These experiments provided data to validate 3-D eddy current codes on geometries with slots or multiple connections.

Analysis of the first series of experiments is appearing elsewhere[3,4] ; this paper describes the analysis of the second and third series. The cantilevered beam experiments are treated in Section 2. Section 3 describes the anaylsis of the cylinder experiments by a fit to two exponentials; and Section 4 the analysis by a transfer function.

## 2. Cantilevered Beam Experiments

In a tokamak fusion reactor or other magnetically confined fusion device, a rapid decay of magnetic field due to a disrupting plasma current induces eddy currents in the limiter and surrounding structures. The eddy currents, through interaction with the applied toroidal and poloidal magnetic fields, produce large mechanical torques and forces that deflect the structural components. Such undesired deformations and the resulting electromagnetic stress may compromise the integrity of the structural design.

Fortunately an important coupling effect between deflection and eddy currents can help mitigate the potential damages to the structures predicted by performing independent electrical and structural analyses. This coupling occurs when, as it deflects, the component intercepts additional magnetic flux. Experiments on the magnetic coupling in rigid body rotation were performed by a team of investigators from PPPL and ANL with FELIX. The results of these experiments [3,4] showed that the coupling between rotation and eddy current could reduce the peak current, deflection and other electromagnetic effects to a level far less severe than would be predicted if coupling is disregarded.

The study of cantilevered beams is the next logical step, and a significant one, beyond the study of moving rigid bodies. Since structures near the plasma are typically cantilevered, the beams provide a better model for the limiter blades of a tokamak fusion reactor than do the rigid body experiments. The beams, which consist of several types of material and have differing dimensions, were clamped rigidly at one end and subjected to simultaneous time-varying and constant magnetic fields. The time-varying field simulates the decaying field during a plasma disruption and the constant field models the toroidal field. The ratios of solenoid to dipole field are kept in a range of 10:1 to 20:1 as would be appropriate to tokamak limiters.

## 2.1 Analytical Model

Consider a cantilever beam of length $\ell_t$, width a and thickness h (Fig. 1) clamped rigidly at one end. Initially everywhere parallel to a uniform and constant magnetic field $B_x$, which in the experiment is called the solenoid field, the beam is also perpendicular to a uniform but time-varying magnetic field $B_y$, which in the experiment is called the dipole field. The time changing field will induce eddy current in the beam. The current in paths parallel to the z direction will interact with constant field $B_x$ and produce a Lorentz force that causes lateral beam deflections in the y direction. As it deflects, the beam will intercept some flux from the field $B_x$. The changing flux produces an additional eddy current that opposes the current produced by the time-varying field and creates a restoring force. Thus the total eddy current is reduced, as is the force from the interaction of the total eddy current and the uniform field.

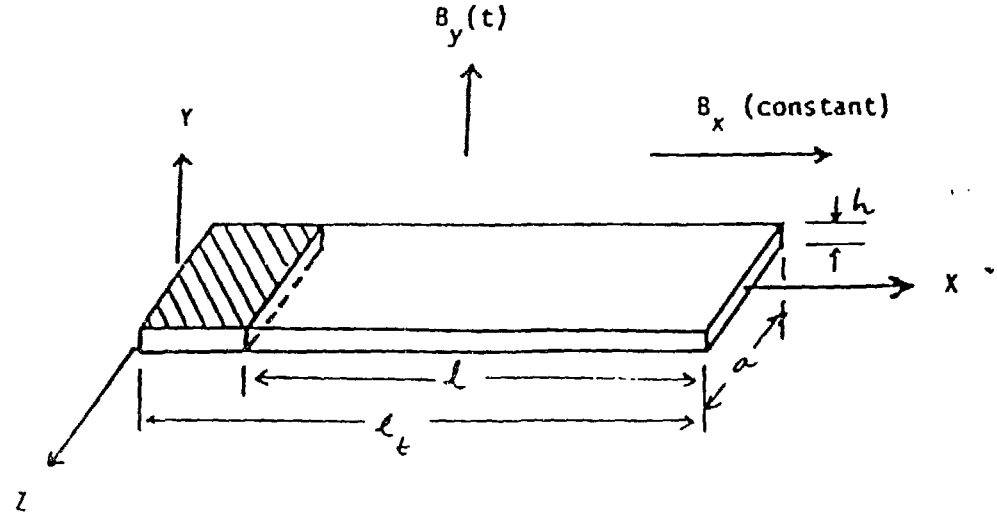


Fig. 1. Schematic of cantilevered beam.

For the purpose of analysis, the current induced in the beam is characterized by a single current loop.

The governing equations can be written as:

$$EI \frac{\partial^4 w(x,t)}{\partial x^4} = p(x,t) - m \frac{\partial^2 w}{\partial t^2} - \frac{\partial w}{\partial t} \tag{1}$$

$$L \frac{dI}{dt} + RI = - \frac{d\phi}{dt} \quad , \tag{2}$$

where:

$w(x,t)$ = the vertical deflection
$EI$ = the flexural rigidity
$m$ = the mass per unit length
$c$ = the mechanical damping constant
$p(x,t)$ = the distributed Lorentz force
$L$ = the effective inductance
$R$ = the effective resistance
$\phi$ = the magnetic flux

$$\phi = - A_t B_y + A B_x \frac{w(\ell,t)}{\ell} \quad . \tag{3}$$

$A_t$ and $A$ are the effective total area and unclamped area of the beam.

In this model $B_y$ decays exponentially from some initial value $B_o$ with decay time constant $\tau_d$

$$B_y(t) = B_o \exp(-t/\tau_d) \tag{4}$$

We assume the general solution for $w(x,t)$ of the form

$$w(x,t) = \sum_{n=1}^{\alpha} X_n(x) f_n(t) \tag{5}$$

where $X_n(x)$'s are the eigenfunctions satisfying the differential equation for free vibration

$$EI \frac{d^4 X_n(x)}{dx^4} = \hat{\omega}_n^2 m X_n \quad ,$$

or

$$\frac{d^4X_n}{dx^4} - k^4X_n = 0 \tag{6}$$

and the four boundary conditions at the fixed end ($x = 0$) and at the free end ($x = \ell$).

The first four eigenvalues $k_n\ell$ and the corresponding eigenmodes of vibration are given in Table 1.

## 2.2 Test Pieces and Measurements

Due to the numerous factors contributing to the coupling effect (damping), several test pieces of various sizes and properties were employed. Half hard copper, phosphor bronze, half hard cartridge brass, and 6061-aluminum alloy were chosen as test materials.

A total of 12 beams with 14 cantilever setups were investigated experimentally. The physical dimensions and properties of the beams are summarized in Table 2. All beams are 48.7 cm long, 10 cm wide, and clamped 7.6 cm from one end unless otherwise stated.

Table 1

EIGENVALUES AND EIGENMODES FOR THE CANTILEVERED BEAM

| n | $k_n\ell$ | Characteristic Modes of Vibration |
|---|---|---|
| 1 | 1.857 | 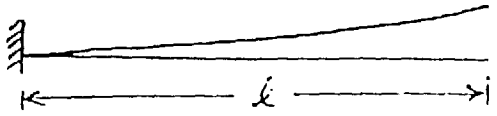  |
| 2 | 4.694 | 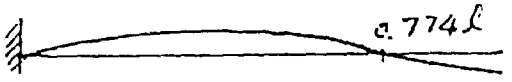  |
| 3 | 7.854 | 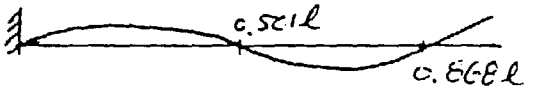  |
| 4 | 10.995 | 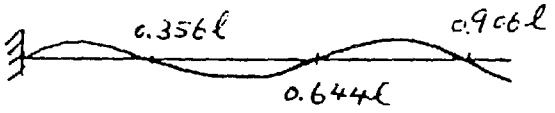  |

The test beams were held rigidly with a nonconducting support frame. Beam deflection was measured with an electro-optical tracking device. The target, which has a light-dark interface, was attached to the edge of the beam at two locations: the free end and 16.7 cm from the end.

The total transient eddy current in the beam was measured with a Rogowski coil linking through a central hole 2.54 cm in diameter.

Strain gauges were used to measure strain and therefore stress in the beam. Strains were measured at two locations, near the clamped end and 16.7 cm from the free end. At each location, a pair of gauges were attached to the top and bottom surfaces of the test beam. The use of double gauges effectively doubles the signal to noise ratio.

The solenoid and dipole fields were measured with a pair of single-axis Hall probes. The probes were excited with a high frequency AC carrier making

them somewhat immune to noise pickup by lead wires.

## 2.3 Dipole Field Alone

When the solenoid field is zero, there is no deflection of the beam, and the circulating current, as measured with the Rogowski coil, experiences a time behavior similar to that described below for the induced field in the cylinder experiments.

Table 2

DIMENSIONAL AND PHYSICAL PROPERTIES OF THE BEAM

| Material | Electrical Resistivity ($\Omega$ -m) | Mass Density ($kg/m^3$) | Young's Modulus (Pa) | Beam # | Thickness (mm) | Remarks |
|---|---|---|---|---|---|---|
| Cu | $1.72 \times 10^{-8}$ | 8912. | $1.1 \times 10^{11}$ | 1 | 2.337 | |
| | | | | 2 | 3.175 | |
| | | | | 3 | 4.597 | |
| Bronze | $1.13 \times 10^{-7}$ | 8857. | $1.1 \times 10^{11}$ | 4 | 3.175 | |
| Brass | $6.10 \times 10^{-8}$ | 8525. | $1.1 \times 10^{11}$ | 5 | 3.175 | |
| Al | $3.95 \times 10^{-8}$ | 2713. | $6.89 \times 10^{10}$ | 6 | 2.350 | |
| | | | | 7 | 3.175 | |
| | | | | 8 | 4.153 | |
| Cu | $1.72 \times 10^{-8}$ | 8912. | $1.1 \times 10^{11}$ | 9 | 3.175 | 9.1cm slot |
| | | | | 10 | 3.175 | 18.2cm slot |
| | | | | 11 | 3.175 | 57.8cm long clamped 16.7cm |
| | | | | 12 | 3.175 | 70.0cm long clamped 28.9cm |

Figure 2 compares the analytic solutions with experimental results for three beams of the same size but of different resistivities: copper, aluminum and brass. In general the analytic prediction agrees well with experimental results. The peak current may differ by up to 10%, but the shape of the predicted curves are preserved.

## 2.4 Combined Dipole and Solenoid Fields

During the combined field tests the solenoid fields used were 0.2, 0.5,

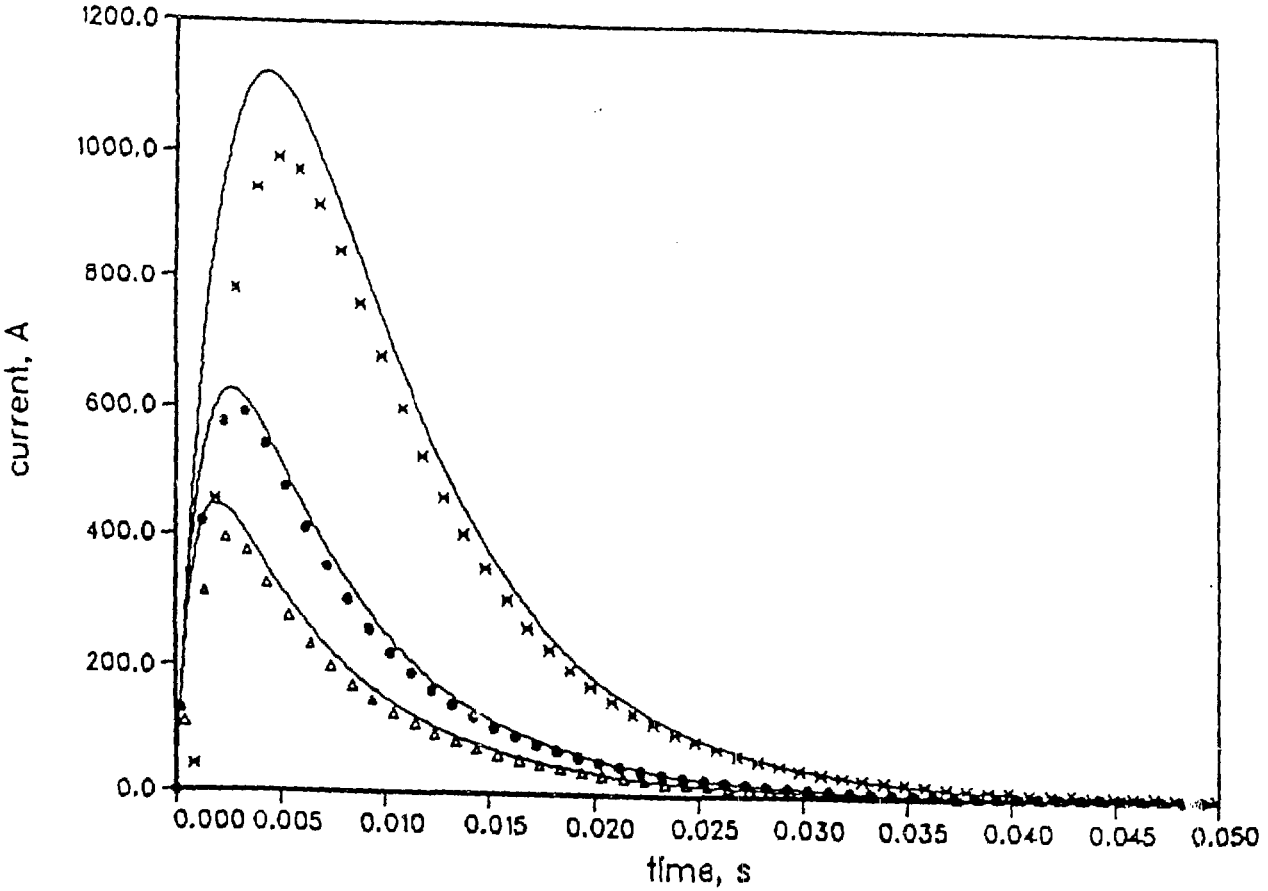


Fig. 2. Current induced in the cantilevered beams. Top to bottom: Copper, Aluminum, brass beams. $B_x = 0$, $B_o = 0.055T$, $\tau_d = 11.6ms$.

0.7 and 0.9 T for each dipole field and decay time. Measurements of the solenoid fields with a horizontal Hall probe when there was no test piece showed the actual fields were close to the nominal values.

Deflection of the beam, through interaction with solenoid field, generates eddy currents that counteract the contributions to the eddy currents resulting from the dipole field decay, and thus can significantly alter the subsequent beam motion. This interaction increases with increasing solenoid field. Figures 2 through 6 show the analytical and experimental results for a medium aluminum beam. In each figure, deflection at the end and 16.7 cm from the end, total eddy current, and strain measured at 3.1 cm and 24.4 cm from the clamped edge are shown. The dipole field was initially 0.055T and decayed exponentially with a time constant of 6.6 ms.

The progression from Fig. 3 to Fig. 6 shows the effect of the coupling. In Fig. 3 ($B_x$ = 0.2T) coupling was weak, the beam oscillated at its natural vibration frequency, the current decayed quite smoothly with only small perturbation due to deflection. The presence of the second mode of vibration could be seen from the strain gauge signal, especially from the gauge located at the middle of the beam. There were practically no contributions from modes higher than the second mode. This observation is consistent with the analytical calculation which predicts higher modes have very little effect on the outcome of the solutions. In Fig. 4 ($B_x$ = 0.5T) the coupling effect became obvious, the second peak in deflection was markedly less than the first peak. The total current decayed faster and a second peak was induced which opposed the beam motion. In Fig. 6 ($B_x$ = 0.9T) the coupling effect was more pronounced. After a first swing, the beam slowly returned to rest at the equilibrium position . It is also interesting to observe that the second mode of vibration was damped more heavily at higher solenoid fields.

Note from Figs. 3 and 6 that the maximum end deflection increased by a factor of 2.1 when the solenoid field increased 4.5 times. Without coupling, the peak deflection would be expected to increase linearly with field intensity. For comparison, the analytical solution without the coupling term are included for the cases of Fig. 3 (weak coupling) and Fig. 6 (strong coupling). See Figs. 7 and 8.

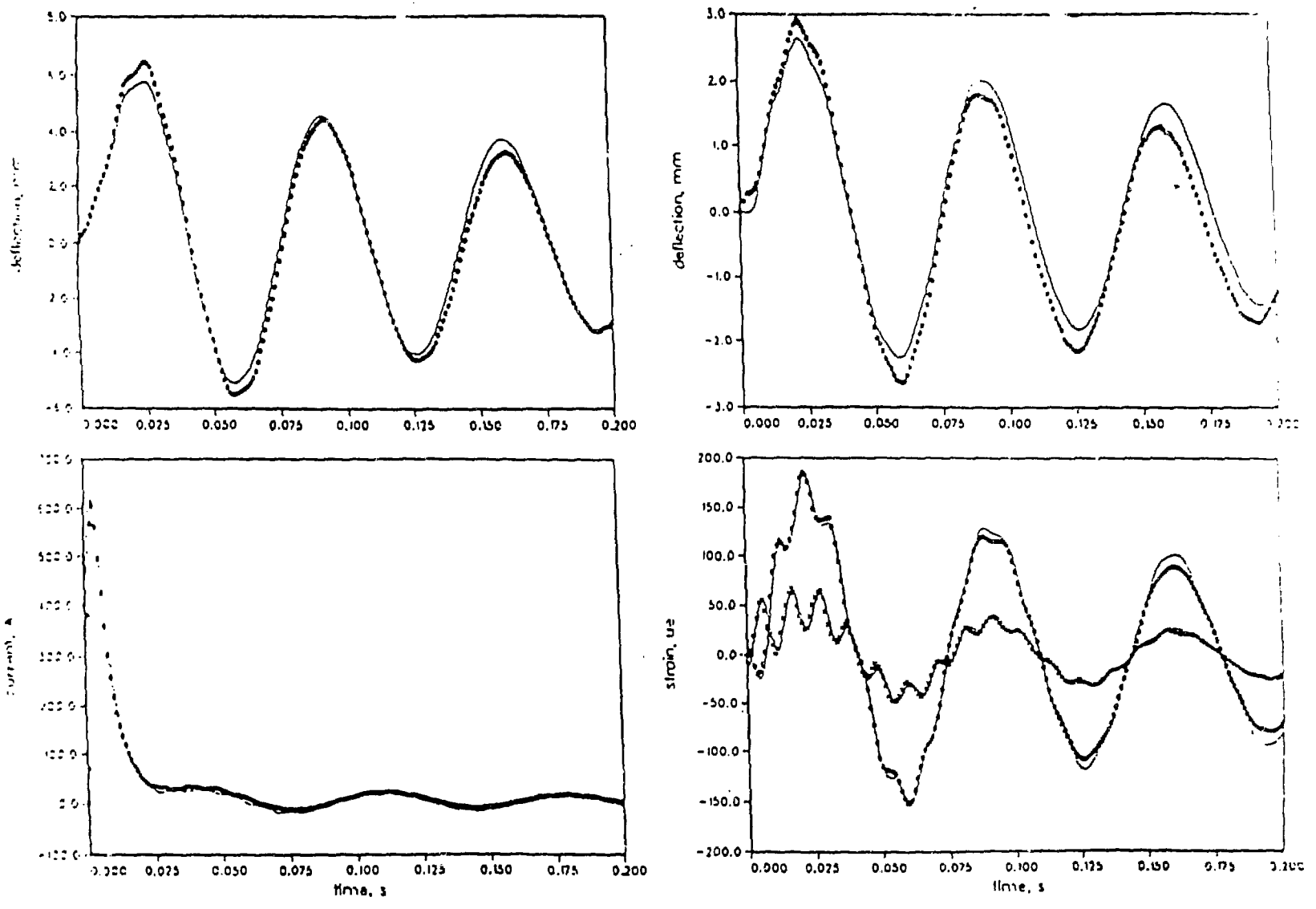


Fig. 3. Current, deflection, and strain in Aluminum beam. $B_x$ - 0.2T, $B_o$ = 0.055T, $\tau_d$ = 6.6 ms.

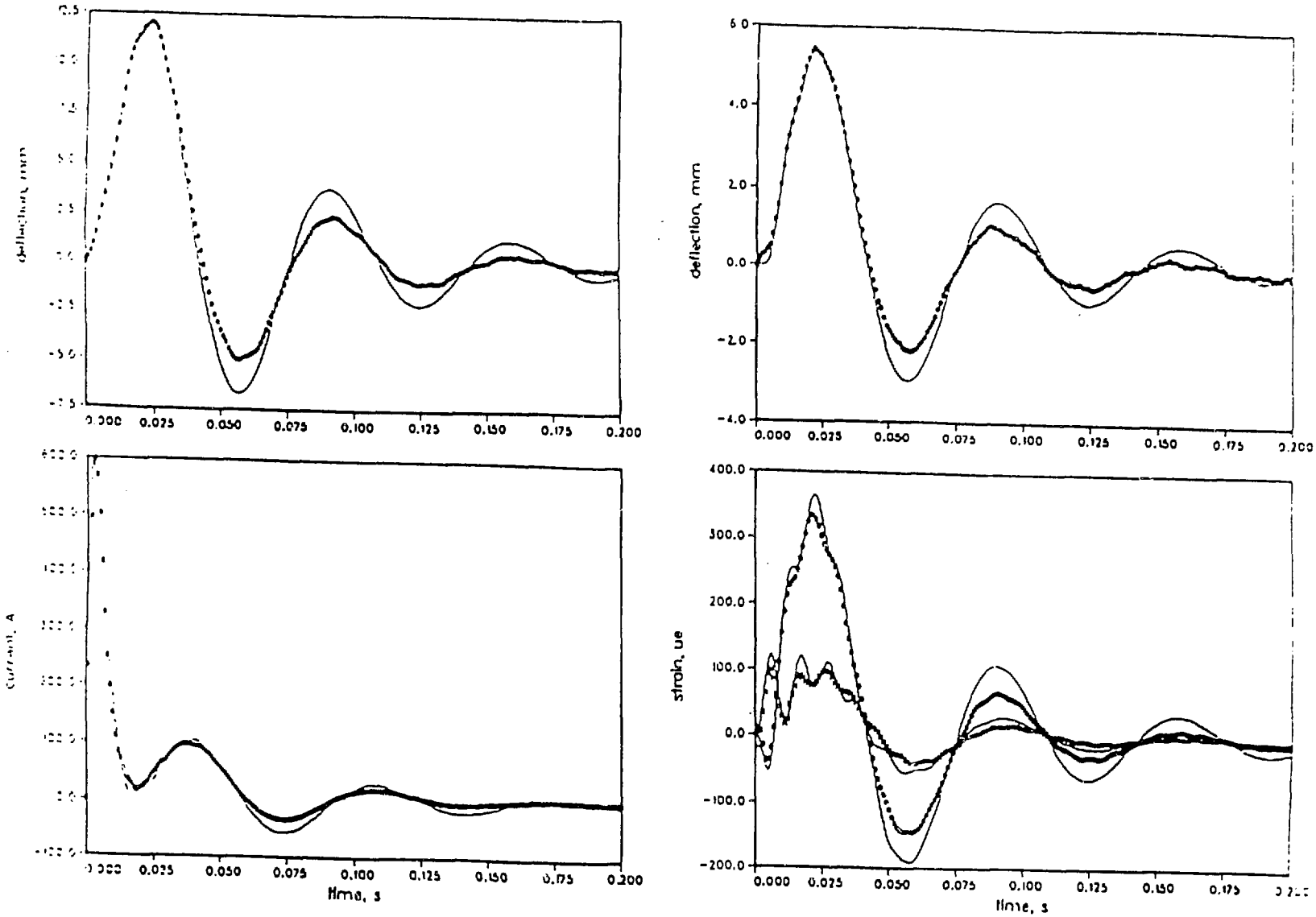


Fig. 4. Current, deflection, and strain in Aluminum beam, $B_x$ = 0.5T, $B_o$ = 0.555T, $\tau_2$ = 6.6 ms.

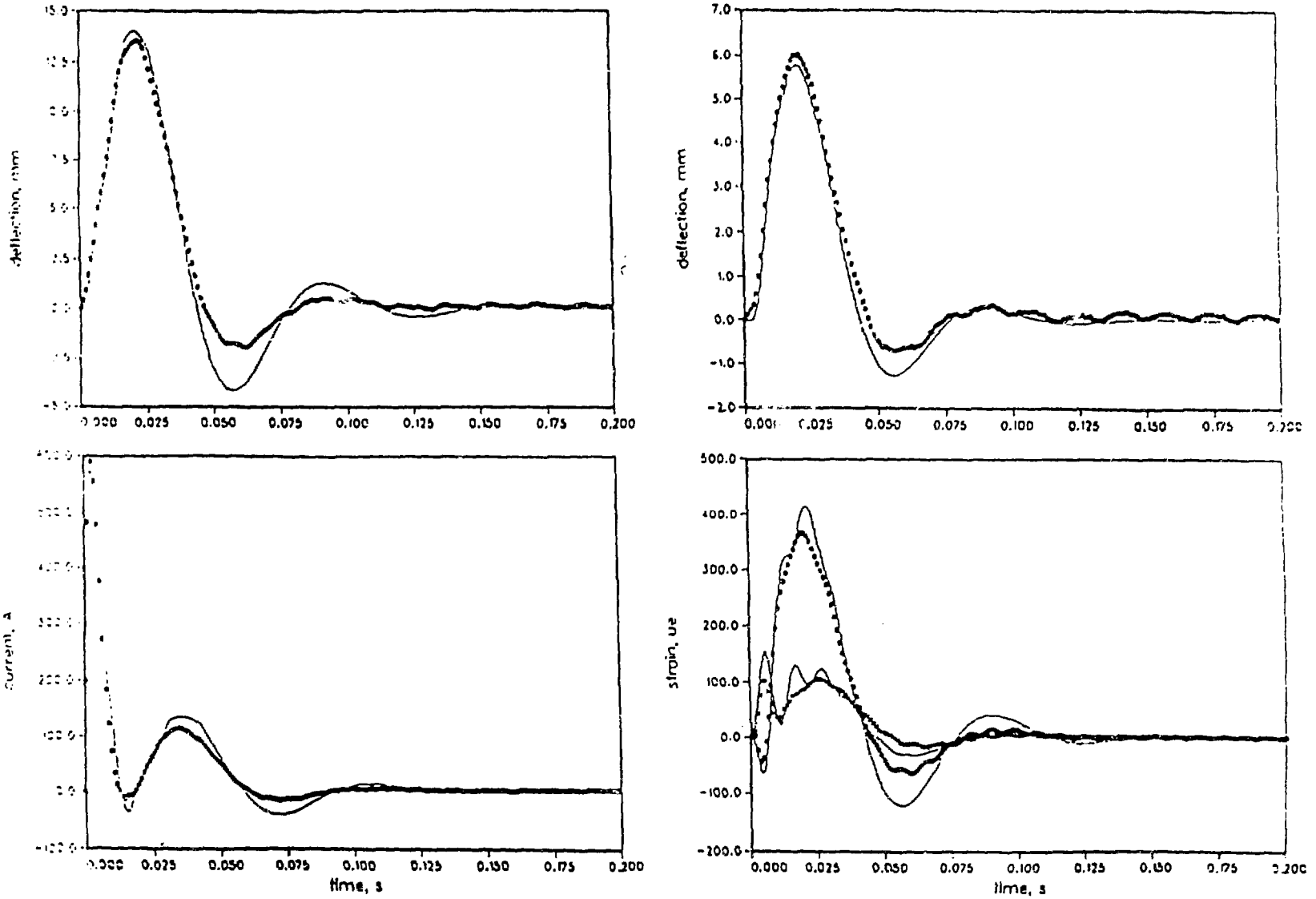


Fig. 5. Current, deflection, and strain in Aluminum beam, $B_x$ = 0.7T, $B_o$ =0.055T, $\tau_2$ = 6.6 ms.

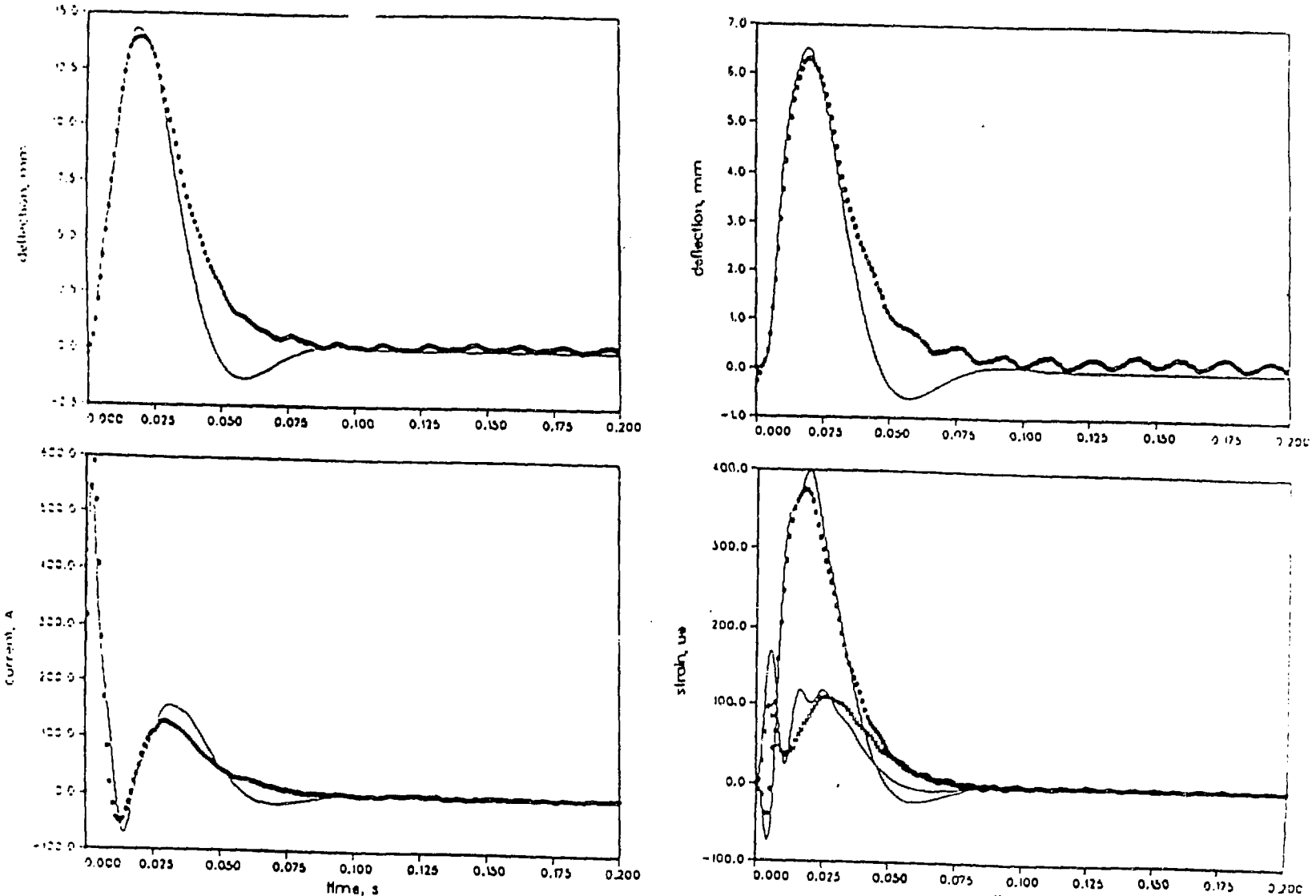


Fig. 6. Current, deflection, and strain in Aluminum beam, $B_x$ = 0.9T, $B_o$ = 0.055T, $\tau_2$ = 6.6 ms.

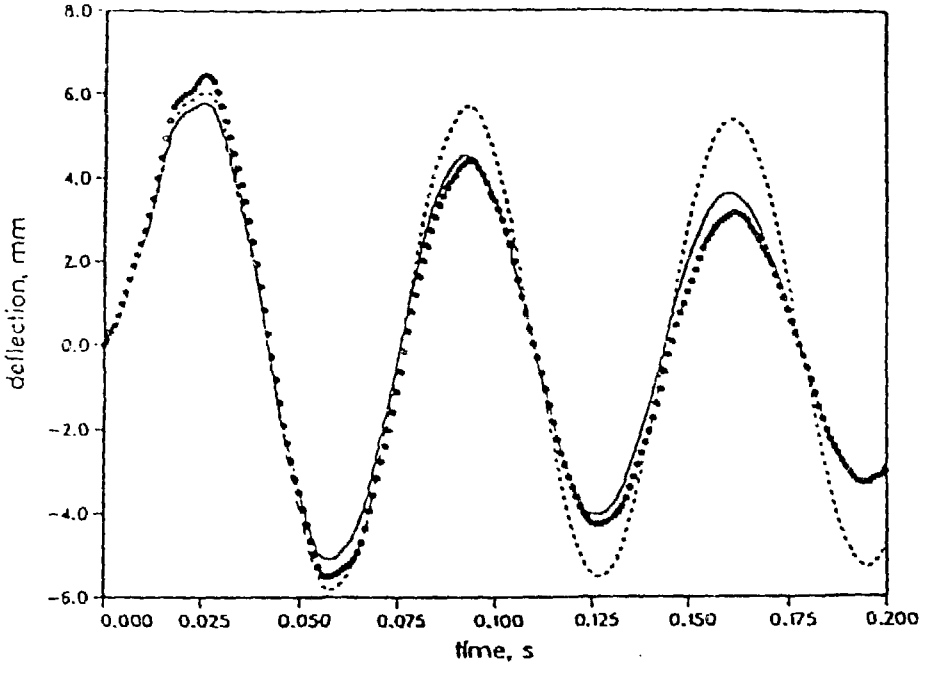


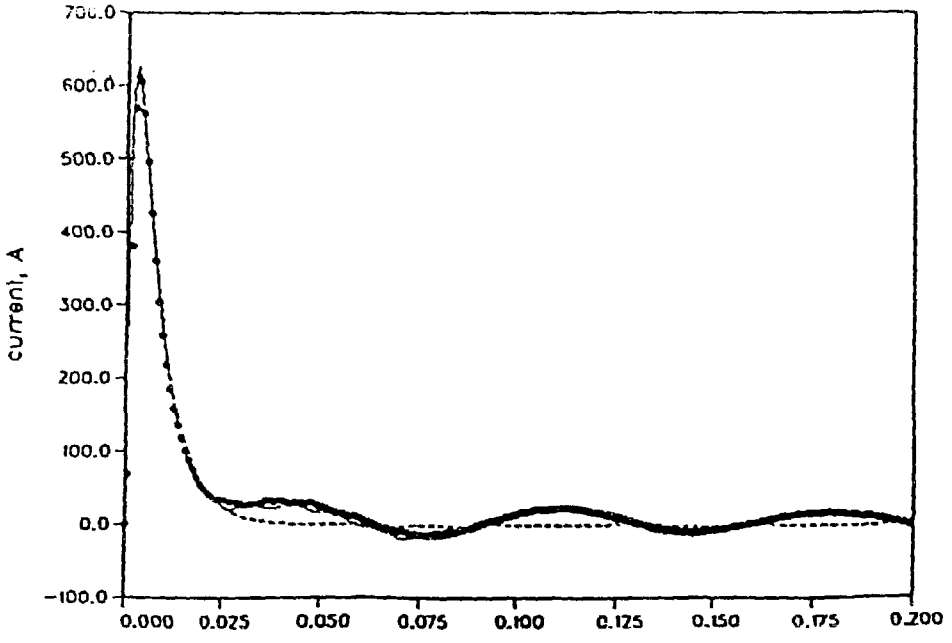


Fig. 7. Deflection and current in aluminum beam. $B_x$ = 0.2T experimental data = dots, uncoupled analysis = dashed line, coupled analysis = solid line.

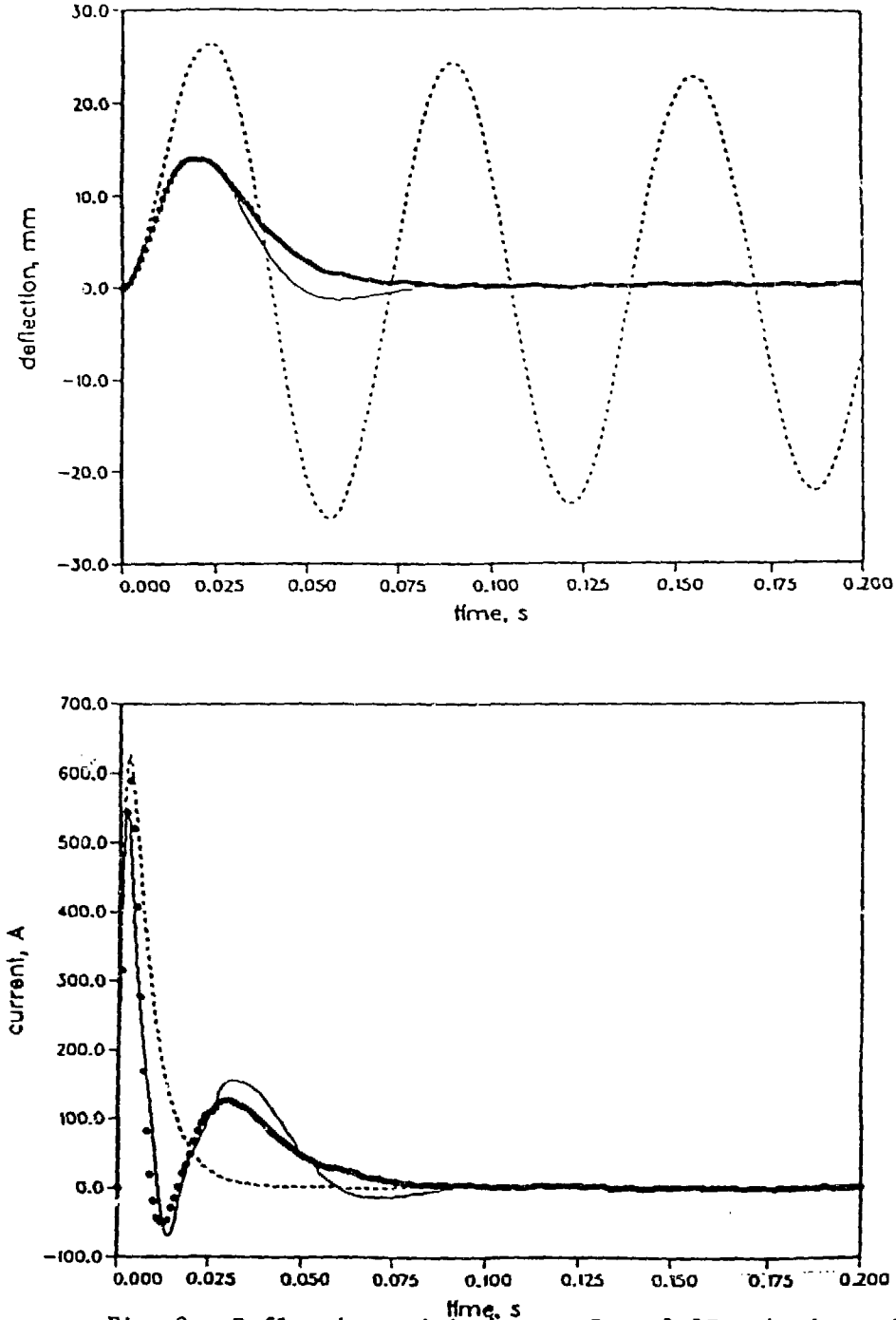


Fig. 8. Deflection and in beam. $B_x$ = 0.9T experimental data = dots, uncoupled analysis = dashed line, coupled analysis = solid line.

## 3. Hollow Cylinder Experiments

A series of experiments was performed to provide data to investigate the limits of applying two-dimensional eddy current codes to three-dimensional geometries. The test pieces were hollow aluminum cylinders with axis horizontal (perpendicular to the dipole field). Each cylinder had two full-length slits located diametrically opposite one another. The slits were located in a horizontal plane, and did not impede the eddy-current flow.

The dimensions of the three cylinders are shown in Table 3. The dimensions were chosen so that all three would have about the same L/R time constant and that the cylinder with the smallest thickness could be approximated closely by a two-dimensional shell, and the other two could be more essentially three-dimensional. The medium cylinder, originally 60 cm long, was later cut into two pieces, 40 cm and 20 cm long.

Table 3

DIMENSIONS OF SPLIT-CYLINDER TEST PIECES

| Test Piece | Length (cm) | Thickness (cm) | O.D. (cm) | I.D. (cm) |
|---|---|---|---|---|
| Large | 120 | 0.48 | 27.3 | 26.34 |
| Medium | 60,40,20 | 1.27 | 13.97 | 11.43 |
| Small | 60 | 2.54 | 10.16 | 5.08 |

Results were presented[5] for the induced field at various axial positions in the large, medium-60 cm, and small cylinders for a nominal dipole field level of 100 mT and nominal decay time of 40 ms. The data was recorded every 2 ms. For completeness, those results are tabulated below.

The analysis described here was primarily for the induced field at various axial positions in the large, medium-40 cm, medium-20 cm, and small cylinders for a nominal dipole field level of 50 mT, nominal decay time of 5 ms, and data recorded every 1 ms. Some date were also obtained and analyzed for the large, medium-40 cm, and medium-20 cm cylinders for a nominal dipole field level of 100 mT, nominal decay time of 10 ms and 40 ms, and data recorded every 1 ms.

The induced field is the difference between the total field and the dipole magnet field, measured by the Hall probe when the cylindrical test

piece is absent. Before the measured dipole magnet field is subtracted, it is normalized by the ratio of the initial total field to initial dipole magnet field, both measured over a 100 ms time period.

An arbitrary time scale is recorded with the data. In general, the time at which the dipole field begins to decay, $t_0$, is taken as an unknown which is to be determined from the data. For convenience, a reference time (550 ms in what follows) is chosen on the arbitrary time scale, and $t_0$ and other times are measured relative to that reference time.

3.1 Fit to Two Exponentials

To put the experimental results in a form convenient to users, they should be expressed by a small number of parameters. One reasonable set of parameters are those of a pair of exponential functions. For the general case, in which the decay begins at an unknown time $t_0$, the induced field B can be written as

$$B = C_1 \exp(-\gamma_1 t) + C_2 \exp(-\gamma_2 t) \qquad (7)$$

The experimental results will be characterized by performing a least-squares fit of Eq. (7) to the data over a suitable time period. However, it is well known that an exponential equation of this type in which all four parameters are to be fitted is extremely ill conditioned.[6]

In general, values or ranges of values are chosen for $\gamma_1$ and $\gamma_2$, and $C_1$ and $C_2$ are determined by a least squares procedure. Figure 9 represents the two-exponential fitting of the induced field at the center of the large cylinder for a nominal 5 ms dipole field decay (actual $\tau$ = 6.87 ms, $1/\tau$ = 0.14556 $ms^{-1}$). The sum of squared deviations (SSD) is given by

$$SSD = \sum_{t=0}^{50} (B_n - B_f^2)$$

where t is the time in 1 ms steps from the reference time, $B_m$ is the measured induced field and $B_f$ is the field from the fit to Eq. (7). The figure shows the values which minimize SSD ($\gamma_1$ = 0.0959 $ms^{-1}$, $\gamma_2$ = 0.1786 $ms^{-1}$), the curve of the $\gamma_1$ which minimizes SSD for specified $\gamma_2$, and the contours for SSD 0.05 $mT^2$ greater and 0.20 $mT^2$ greater than the mimimum value, 1.237 $mT^2$.

As can be seen in the figure, large changes in $\gamma_1$ and $\gamma_2$ along the minimum curve will result in only a small increase in SSD.

Analysis of the cylinder experiments with a time constant of 40 ms[5]

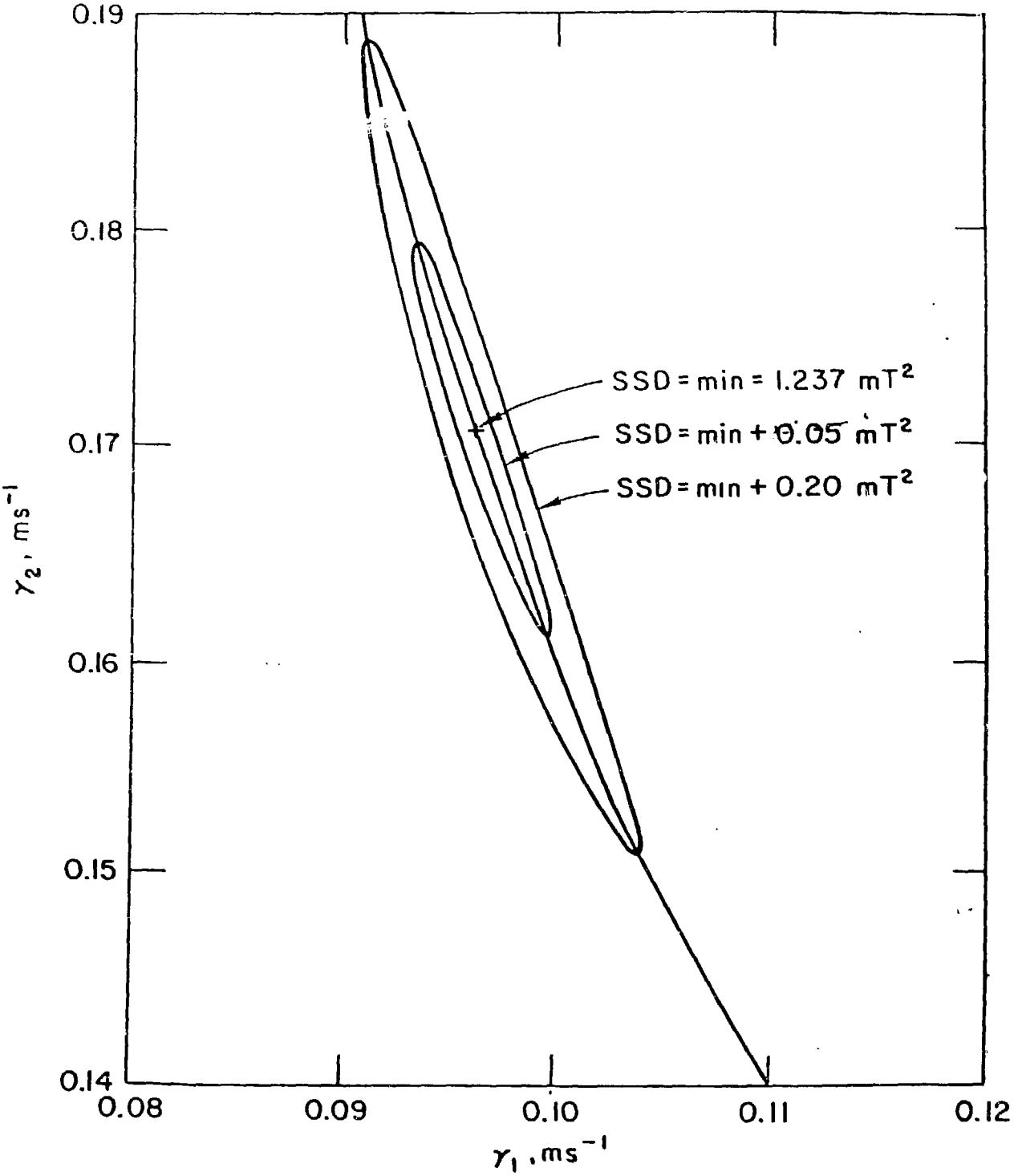


Fig. 9. Sum of squared deviations (SSD) for fit of induced field by two exponentials, showing the values which minimize SSD ($\gamma_1$ = 0.0959 ms$^{-1}$, $\gamma_2$ = 0.1786 ms$^{-1}$), the curve of the $\gamma_1$ which minimizes SSD for specified $\gamma_2$, and the contours for SSD 0.05 mT$^2$ greater and 0.20 mT$^2$ greater than the mimimum value, 1.237 mT$^2$. $\tau$ = 6.87 ms, 0 cm position.

showed that the induced field B could be fit Eq. (7) and that $\gamma_1$ and $\gamma_2$ could be identified as the reciprocals of the applied field decay time $\tau$ and the test-piece L/R time. For $\gamma_1 = 0.0252\ ms^{-1}$, as determined from the data with no test piece, a three-parameter fit for $\gamma_2$, $C_1$, and $C_2$ yielded values of $\gamma_2$ for different axial positions in a given cylinder that varied up to 10% with one another as shown in Table 4. A four-parameter fit to the large cylinder data for $\tau = 6.87$ ms; shows that both $\gamma_1$ and $\gamma_2$ vary with position, and neither of them is near $\gamma_0 = 1/\tau = 0.14556\ ms^{-1}$.

Table 4

TWO EXPONENTIAL FIT TO INDUCED FIELD IN THE LARGE CYLINDER $\tau$ = 39.68ms

$\gamma_1 = 0.0252\ ms^{-1}$

| Position | cm | 0 | 10 | 20 | 30 | 40 | 45 | 50 |
|---|---|---|---|---|---|---|---|---|
| $\gamma_2$ | $ms^{-1}$ | 0.0977 | 0.0960 | 0.0942 | 0.1000 | 0.10785 | 0.1110 | 0.0973 |
| $C_1$ | mT | 25.67 | 23.536 | 22.25 | 27.30 | 18.26 | 15.30 | 9.983 |
| $C_2$ | mT | -20.41 | -18.19 | -17.17 | -21.04 | -14.05 | -11.40 | -7.169 |
| C | mT | 27.800 | 25.797 | 24.459 | 29.804 | 19.779 | 16.681 | 11.132 |
| $t_o$ | ms | -3.163 | -3.639 | -3.756 | -3.482 | -3.171 | -3.429 | -4.523 |
| $t_m - t_o$ | ms | 18.690 | 18.891 | 19.110 | 18.427 | 17.591 | 17.281 | 18.737 |
| $B_m$ | mT | 12.880 | 11.819 | 11.069 | 14.012 | 9.730 | 8.342 | 5.144 |
| $B_o$ | mT/ms | 2.005 | 1.826 | 1.688 | 2.229 | 1.635 | 1.431 | 0.802 |
| $B_o'$ | | 2.925 | 2.919 | 2.914 | 2.932 | 2.956 | 2.965 | 2.923 |

TWO EXPONENTIAL FIT, MEDIUM & SMALL CYLINDER $\tau$ = 39.68 ms

$\gamma_1$ = 0.0252 $ms^{-1}$

| Position | cm | Medium 0 | Medium 10 | Medium 20 | Small 0 | Small 10 | Small 20 |
|---|---|---|---|---|---|---|---|
| $\gamma_2$ | $ms^{-1}$ | 0.0778 | 0.0791 | 0.0864 | 0.0741 | 0.0743 | 0.0823 |
| $C_1$ | mT | 48.465 | 48.323 | 35.298 | 51.059 | 48.991 | 47.898 |
| $C_2$ | mT | -41.474 | -41.46 | -28.77 | -43.888 | -41.91 | -42.1 |
| C | mT | 52.220 | 51.911 | 38.399 | 55.201 | 53.078 | 50.705 |
| $t_o$ | ms | -2.962 | -2.842 | -3.341 | -3.095 | -3.179 | -2.260 |
| $t_m-t_o$ | ms | 21.431 | 21.222 | 20.133 | 22.057 | 20.022 | 20.727 |
| $B_m$ | mT | 20.573 | 20.721 | 16.376 | 20.895 | 20.137 | 20.866 |
| $B_o$ | mT/ms | 2.747 | 2.798 | 2.350 | 2.699 | 2.606 | 2.895 |
| $B_o'$ | | 2.861 | 2.866 | 2.889 | 2.849 | 2.850 | 2.876 |

Table 5

TWO EXPONENTIAL FIT TO INDUCED FIELD IN LARGE CYLINDER

$\gamma_c = 0.14556\ ms^{-1}$, $\tau = 6.87$ ms

| Position | cm | 0 | 10 | 20 | 30 | 40 | 45 | 55 |
|---|---|---|---|---|---|---|---|---|
| $\gamma_1$ | $ms^{-1}$ | 0.0959 | 0.0967 | 0.0993 | 0.1016 | 0.1005 | 0.1026 | 0.1060 |
| $\gamma_2$ | $ms^{-1}$ | 0.1706 | 0.1669 | 0.1689 | 0.1733 | 0.1972 | 0.2077 | 0.2203 |
| $C_1$ | mT | 79.67 | 82.40 | 76.47 | 100.61 | 45.34 | 43.95 | 13.11 |
| $C_2$ | mT | -61.36 | -63.69 | -60.17 | -70.24 | -33.63 | -30.37 | -10.83 |
| C | mT | 111.37 | 117.49 | 107.64 | 100.61 | 61.85 | 63.06 | 15.65 |
| $t_o$ | ms | 0.53 | 0.35 | 0.58 | 0.48 | 0.93 | 0.50 | 2.35 |
| $t_m - t_o$ | ms | 7.71 | 7.78 | 7.63 | 7.45 | 6.97 | 6.71 | 6.40 |
| $t_m$ | ms | 8.24 | 8.13 | 8.21 | 7.93 | 7.90 | 7.21 | 9.75 |
| $B_m$ | mT | 23.28 | 23.30 | 20.79 | 19.53 | 15.06 | 16.03 | 4.12 |
| $\dot{B}_o$ | mT/ms | 8.322 | 8.246 | 7.493 | 7.211 | 5.983 | 6.626 | 1.789 |
| $\dot{B}_o'$ | | 2.756 | 2.752 | 2.750 | 2.750 | 2.770 | 2.774 | 2.779 |
| SSD | $mT^2$ | 1.237 | 1.558 | 1.492 | 0.725 | 1.105 | 1.942 | 1.089 |

Since different values of $\gamma_1$ and $\gamma_2$ fit the experimental data for induced field almost equally well, as seen in Fig. 9, it seems worthwhile to seek unique parameters to characterize the data.

Four parameters with more physical significance are shown in Fig. 10: $t_o$, the initial time, at which B = 0; $\dot{B}_o$, the rate of change of B at $t_o$; $t_m$, the time at which B is a maximum; and $B_m$, the field at $t_m$. These four parameters ($t_o$, $t_m$, $B_m$, $\dot{B}_o$) can be expressed in terms of ($\gamma_1$, $\gamma_2$, $C_1$, $C_2$). The values of $\gamma_2$, $C_1$, and $C_2$ which give the best fit vary strongly with $\gamma_1$, but the values of ($t_o$, $t_m$, $B_m$, $\dot{B}_o$) calculated from ($\gamma_1$, $\gamma_2$, $C_1$, $C_2$) vary only slowly.

The two-exponential expression, Eq. (7) can be rewritten as:

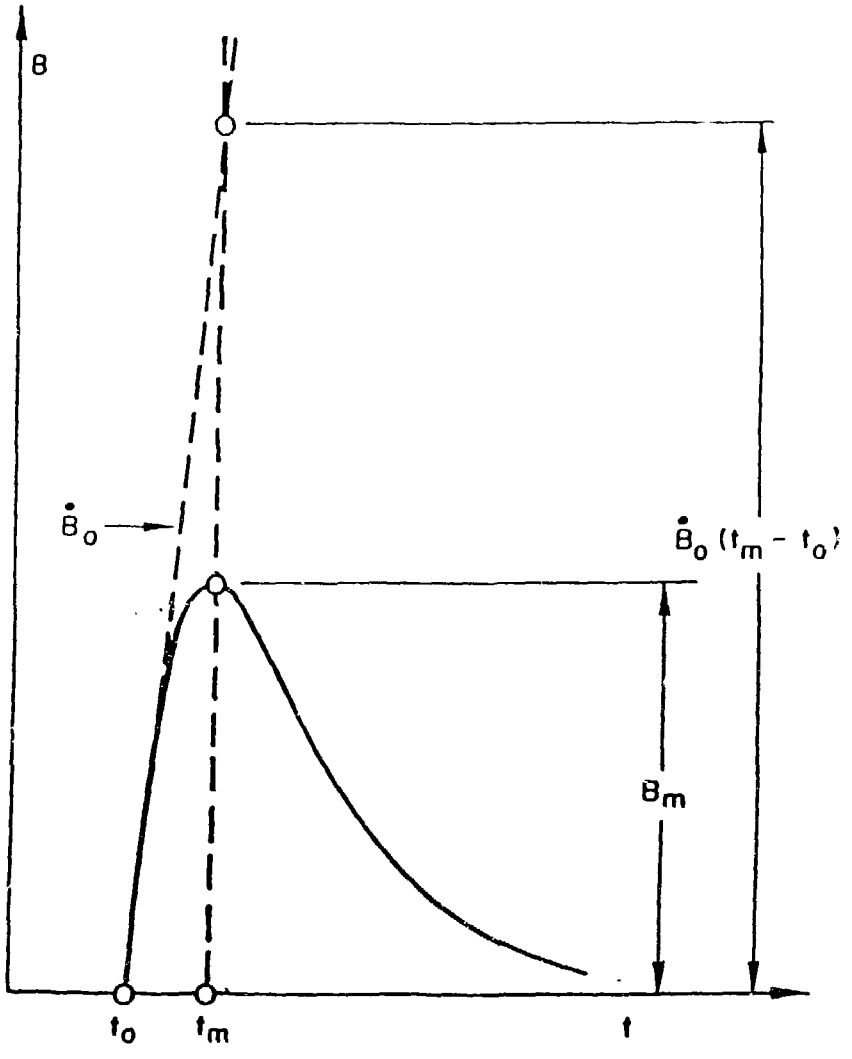


Fig. 10. Four physical parameters characterizing the induced field data.

$$B = C\,[\exp\{-\gamma_1 (t - t_o)\} - \exp\{-\gamma_2 (t - t_o)\}] \tag{8}$$

with

$$t_o = \ln(-C_2/C_1)/(\gamma_2 - \gamma_1) \tag{9}$$

$$C = C_1 \exp(-\gamma_1 t_o) = -C_2 \exp(-\gamma_2 t_o) \tag{10}$$

Differentiating Eq. (8), we find

$$t_m - t_o = \ln(\gamma_1/\gamma_2)/(\gamma_1 - \gamma_2) \tag{11}$$

$$B_m = C\,(1 - \gamma_1/\gamma_2) \exp\{-\gamma_1 (t_m - t_o)\} \tag{12}$$

$$\dot{B}_o = C\,(\gamma_2 - \gamma_1) \tag{13}$$

Combining Eq. (11) - (13) yields the result that the dimensionless form $\dot{B}_o'$ obeys

$$\dot{B}_o' \equiv \dot{B}_o\,(t_m - t_o)/B_m = e \text{ if } \gamma_1 = \gamma_2 \tag{14}$$

$$> e \text{ if } \gamma_1 \neq \gamma_2$$

Tables 4 and 5 show the values of these physical parameters.

## 3.2 Three Exponential Fit

If the cylinder displayed a single eddy-current mode, then $\gamma_1$, $\gamma_2$, $t_m$, and $t_o$ would not vary with axial position. The observed variation suggests that more than one eddy current mode is active. If two are acting, then the data might be better fit by:

$$\begin{aligned} B = {} & C_a[\exp\{-\gamma_a(t-t_o)\} - \exp\{-\gamma_o(t-t_o)\}] \\ & + C_b[\exp\{-\gamma_b(t-t_o) - \exp\{-\gamma_o(t-t_o)\}] \end{aligned} \tag{15}$$

In the two current mode model, the values of $C_a$ and $C_b$ would be expected to vary with axial position, but the values of the $t_o$, $\gamma_o$, $\gamma_a$ and $\gamma_b$ would not. In practice the fit with Eq. (15) was never appreciably better than the

fit with Eq. (7), and good fit required $\gamma_a$, $\gamma_b$, $\gamma_o$, and/or $t_o$ to vary with axial position. Such behavior is inconsistent with a model of two dominant eddy current modes, but could be consistent with several dominant modes.

## 4. Transfer Function Analysis

The electromagnetic behavior of the cylinder can be thought of as a linear system which generates an output g(t), i.e. the induced field, from an input f(t). The time derivative of the dipole field without the test piece is considered as the input. The transfer function $H(\omega)$ characterizes the system and is given by

$$H(\omega) = G(\omega)/F(\omega) \tag{16}$$

where $F(\omega)$ and $G(\omega)$ are the Fourier transforms of input f(t) and output g(t), respectively.[7] The transfer function is unique and independent of the input. Once the transfer function has been calculated, the output from any input is calculated from the inverse-Fourier transfer of $H(\omega)\ F(\omega)$, or the convolution of input f(t) and system impulse response h(t). The impulse response h(t) is the response of the system when the input is a delta function $\delta(t)$; it is calculated as the inverse-Fourier transform of $H(\omega)$.

To better understand the electromagnetic induction mechanism and put the experimental results in a form convenient for comparison with the results of eddy-current code computation, the transfer function $H(\omega)$ is analyzed in terms of its pole(s). If the electromagnetic induction does not incorporate any capacitance, the poles are located on the positive pure-imaginary axis, and correspond to an exponentially decaying impulse response. From a real system condition, i.e. $H(\omega) = H^*(-\omega)$, the coefficients of the poles are also pure imaginary and the transfer function may be written as

$$H(\omega) = \sum_{n=1}^{\infty} -iC_n/(\omega - i\,\gamma_n) \tag{17}$$

where $\gamma_n$ and $C_n$ are real numbers.

For an exponentially decaying function with time constant $\tau_o \equiv 1/\gamma_o$, i.e. $f(t) = f_o\, e^{-\gamma_o t}$, as input, the transfer function Eq. (17) is equivalent to an induced field

$$g(t) = \sum_{n=1}^{\infty} \frac{f_o C_n}{\gamma_o - \gamma_n} \left[\exp(-\gamma_n t) - \exp(-\gamma_o t)\right] .$$

In the case of a single pole (n=1 only),

$$g(t) = \frac{f_o C_1}{\gamma_o - \gamma_1} \left[\exp(-\gamma_1 t) - \exp(-\gamma_o t)\right] .$$

## 4.1 Transfer Functions with One Pole

If the test cylinder is characterized by a single L/R time constant, the transfer function will have only one pure-imaginary pole; i.e.

$$H(\omega) = H_r(\omega) + iH_i(\omega) = -iC/(\omega - i\gamma) = C(\gamma - i\omega)/(\omega^2 + \gamma^2) \qquad (18)$$

where $\gamma$ and C are real values identifying the location and amplitude of the pole, and $H_r(\omega)$ and $H_i(\omega)$ are the real and imaginary parts of $H(\omega)$, respectively. As shown in Fig. 2(a) this one-pole transfer function is best characterized by the maximum of $H_r$ at $\omega = 0$, and minimum and maximum of $H_i$ at $\omega = \pm\gamma$. It is worth noticing that $|H_r(0)| = 2|H_i(\pm\gamma)| = C/\gamma$. Another important characteristic of one-pole transfer functions is that the real and imaginary parts of its reciprocal, $G(\omega) \equiv 1/H(\omega)$ are constant ($\gamma/C$) and linear ($\omega/C$), respectively (Fig. 11).

Therefore, provided the reciprocal of the transfer function calculated from experimental data shows constant real part and linear imaginary part, the transfer function has only one pole $\gamma = G_r/(G_i'/d\omega)$ and coefficient $C = (G_i'/d\omega)^{-1}$, where $G_r$ and $G_i'$ are the real part and the derivative of the imaginary part of $1/H(\omega)$, respectively.

## 4.2 Transfer Functions with Two Poles

If the test cylinder has two distinct current patterns with different time constants, the transfer function may also have two pure-imaginary poles, corresponding to the two time constants, as

$$H(\omega) = H_r(\omega) + i\,H_i(\omega) = \frac{-iC_1}{\omega - i\gamma_1} + \frac{-iC_2}{\omega - i\gamma_2}$$

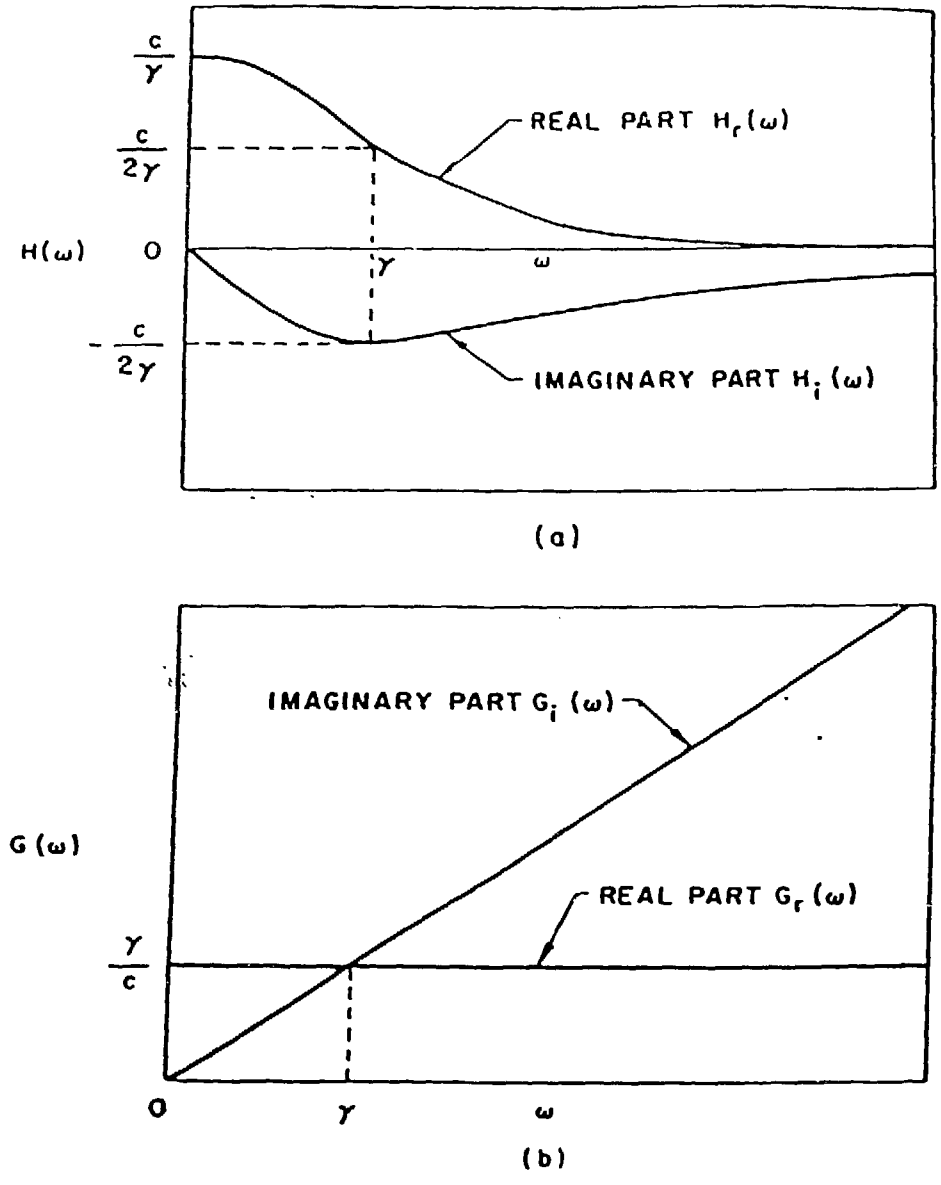


Fig. 11. (a) One pole transfer function $H(\omega)$, and (b) its reciprocal $G(\omega) = 1/H(\omega)$

$$= \left[\frac{C_1 \gamma_1}{\omega^2 + \gamma_1^2} + \frac{C_2 \gamma_2}{\omega^2 + \gamma_2^2}\right] - i\omega \left[\frac{C_1}{\omega^2 + \gamma_1^2} + \frac{C_2}{\omega^2 + \gamma_2^2}\right] , \tag{19}$$

and its reciprocal becomes

$$1/H(\omega) = G(\omega) = G_r(\omega) + i\, G_i(\omega) = \frac{1}{C}\left[A - \frac{DB}{\omega^2 + B^2}\right] + i\,\frac{\omega}{C}\left[1 + \frac{D}{\omega^2 + B^2}\right] , \tag{20}$$

where

$$A = \frac{C_1\gamma_1 + C_2\gamma_2}{C_1 + C_2} \quad , \quad B = \frac{C_1\gamma_2 + C_2\gamma_1}{C_1 + C_2} ,$$

$$C = C_1 + C_2 \quad , \quad D = \frac{(\gamma_1 - \gamma_2)^2}{(C_1 + C_2)^2}\, C_1\, C_2 .$$

Now $G_r$ is no longer constant, except in the limits of small $\omega$, $|\omega| << |B|$, and large $\omega$, i.e. $|\omega| >> |D|$. Also $G_i$ is linear in the same limits (Fig. 12). Therefore, from the values of $G_r(0)$, $G_r(\infty)$, $G_i'(0)$, and $G_i'(\infty)$, one can calculate poles and their coefficients. However, accuracy of the transfer function calculation at high frequencies is hard to achieve, especially from experimental data with substantial noise and low sampling rate.

A more practical method starts with approximate values for one pole. Under the assumption that $i\gamma_1$ is a pole of the transfer function, the other pole and coefficients can be calculated as

$$\gamma_2 = \frac{H_r(\gamma_1) + H_i(\gamma_1)}{H_r(\gamma_1) - H_r(0) - H_i(\gamma_1)}\, \gamma_1 , \tag{21a}$$

$$C_2 = \frac{\gamma_2^2}{\gamma_2 - \gamma_1}\, [H_r(0) + \gamma_1\, H_i'(0)] , \tag{21b}$$

and

$$C_1 = \gamma_1\, [H_r(0) - C_2/\gamma_2] . \tag{21c}$$

Also $\gamma_1$ should satisfy an equality such as

$$\frac{[H_r(\gamma_1) - H_r(0) - H_i(\gamma_1)]^2}{H_r(\gamma_1) + H_i(\gamma_1)} - H_r(0) + H_r(\gamma_1) + H_i(\gamma_1) = \gamma_1\, H_i'(0) . \tag{22}$$

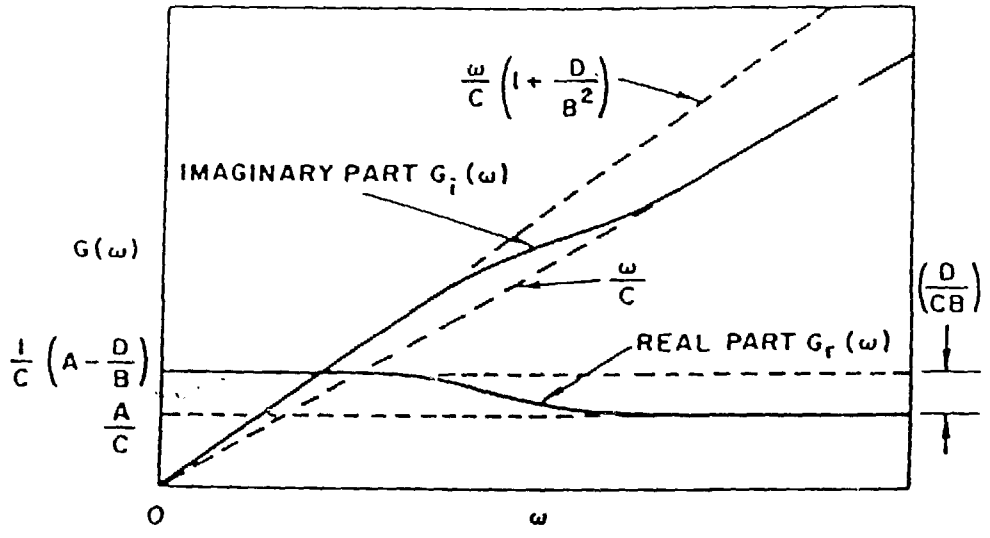


Fig. 12. Reciprocal of the transfer function, $G(\omega) = 1/H(\omega)$, with two pure imaginary poles.

In actual data analysis one may need to iterate to satisfy Eq. (22) and/or the condition of minimum standard deviation between experimental data and the two-pole-fit data.

## 4.3 Analysis Procedure

Transfer functions from FELIX cylinder experiments are analyzed for several axial positions. Four different cylinders, i.e. large cylinder, medium cylinders with 40 cm and 20 cm length, and small cylinder, all with horizontal slits, are used for the experiment. Experimental data with 5 ms (nominal) dipole decay time constant are selected to investigate axial-position dependence of the transfer functions. Also several data with 10 ms and 40 ms nominal dipole decay time constant are analyzed to check the independence of the transfer function from input.

First the actual time constants of input dipole field were calculated. The Fourier transforms of the dipole field without any test piece show characteristics of one-pole transfer function as described in the previous section and Fig. 11. Actual time constants turn out to be 6.87, 12.03, and 39.40 ms for nominal 5, 10, and 40 ms data, respectively. Then the input is calculated as

$$F(\omega) = i\, B_0\, \gamma_0/(\omega - i\, \gamma_0) ,$$

where $\gamma_0$ and $B_0$ are time constant and field magnitude at $t = 0$, respectively. Note that the time differentiation of the dipole field has contributed a factor of $\gamma_0$ on $F(\omega)$. This analytic input was used in all subsequent analysis.

For each set of experimental data a transfer function is calculated from the Fourier transform of the induced field and $F(\omega)$, and is fitted to the one-pole representation. Since the sum of squared deviations between the calculated transfer function $H(\omega)$ and one-pole fitted $\bar{H}(\omega)$ varies very rapidly with small changes in the zero-time $t_0$, the transfer function was multiplied by $\exp(i\omega\, \Delta t_0)$ to best-fit the one-pole representation. The $\Delta t_0$ values, less than 1 ms for FELIX experimental data, may be an indication of uncertainty in experimental dipole-discharge zero times. Then Eqs. (21) and (22) are applied using the one-pole as $\gamma_1$, to determine if there is a second pole, and if so,

to determine its location and its coefficient. Also the real and imaginary parts of the $1/H(\omega)$ are examined for characteristics of a two-pole transfer function.

## 4.4 Results

Over the central region of each cylinder, the induced signal is strong enough to permit the transfer function analysis. However near the ends the induced field is too weak to find a meaningful transfer function.

Figure 13 shows the transfer function and its reciprocal at the center of the medium (40 cm) cylinder. The real part of $1/H(\omega)$ is close to constant, and the one-pole representation of the transfer function is almost identical to the one calculated from experimental data. Hence the amplitude of the second pole is very small compared to the first pole, and the two-poles representation is nearly the same as the one-pole representation except for very small $\omega$.

Near the ends of the cylinders the induced field is weak, and the difference between actual data and one-pole fit becomes prominent for small $\omega$ as shown in Fig. 14. The two pole fit gives better results for small $\omega$, but is almost identical for others. However the second pole is still very weak and small, and may come from experimental errors.

Results of the fittings are summarized in Tables 6-9. The values of $\Delta t_o$ in the tables are measured from the beginning of the range used for the Fourier transform.

The variation of the dominant pole values with axial position for each cylinder is shown in Fig. 15. Poles of 6.87 ms dipole decay time are connected by lines. Other poles of 12.03 and 39.40 ms data are also shown for comparison, and support the independence of the transfer functions from the input field. It is worth noticing that the pole becomes bigger, i.e. the induced field decays more rapidly, as its position approaches the ends of the cylinders. This interesting phenomena may indicate the existence of many eddy current modes in the cylinders. Also the pole amplitude becomes smaller as its axial position approaches the cylinder ends.

The sum of squared deviations divided by the sum of the square of the transfer function, i.e. $\Sigma\,[H(\omega) - \bar{H}(\omega)]^2 / \Sigma\, H^2(\omega)$ exhibits steep minima as a

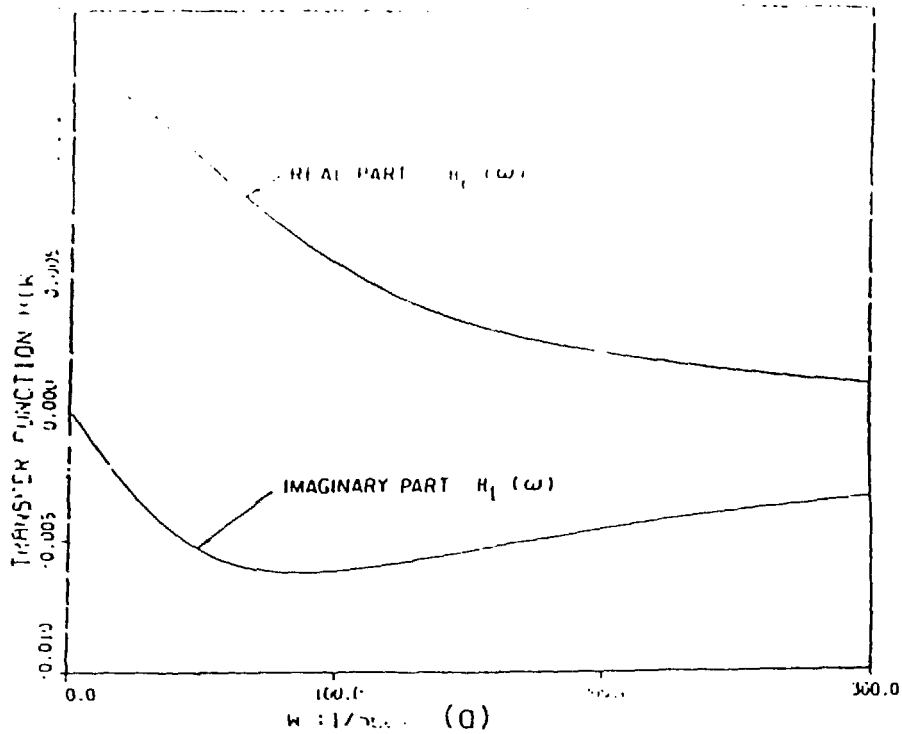


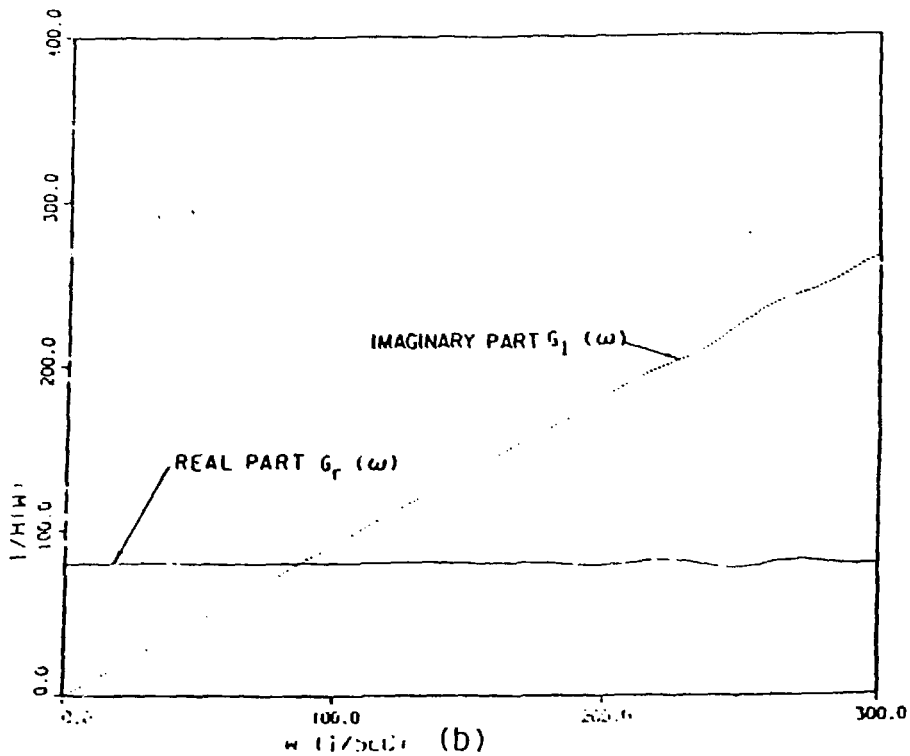


Fig. 13.

(a) Transfer function $H(\omega)$ at x = 0 cm for the medium 40 cm cylinder, as a function of $\omega$. Dotted line is calculated from FELIX data, and the two solid lines are one pole and two pole representations. One pole and two pole fits are almost identical except for very small $\omega$, where two pole fit gives better results.

(b) Reciprocal of the transfer function at same condition. Real part is constant and imaginary part is linear for $|\omega| < 180\ s^{-1}$.

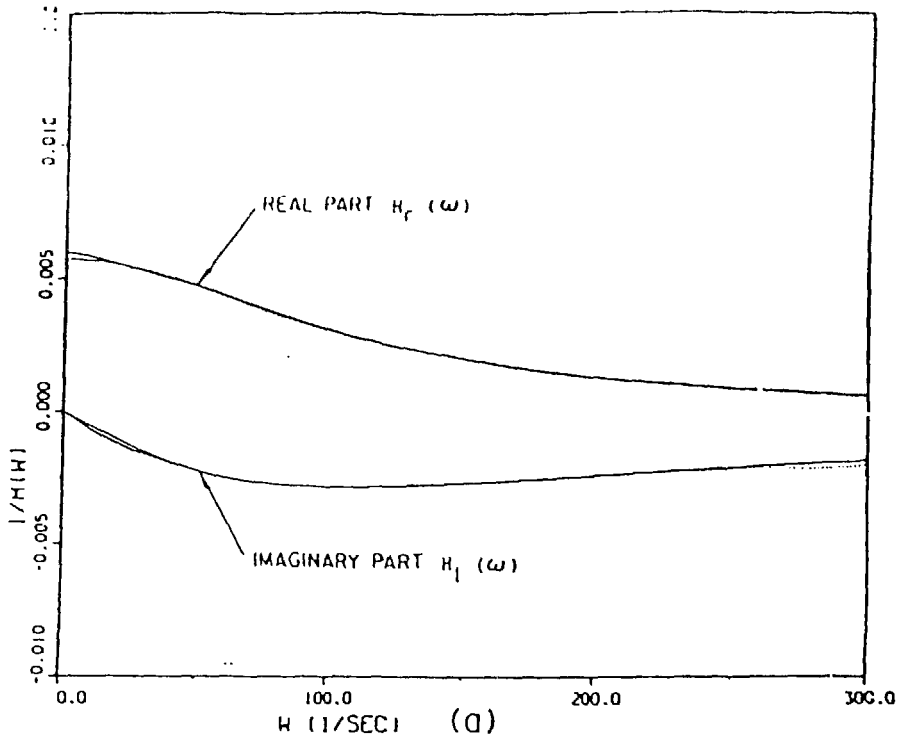


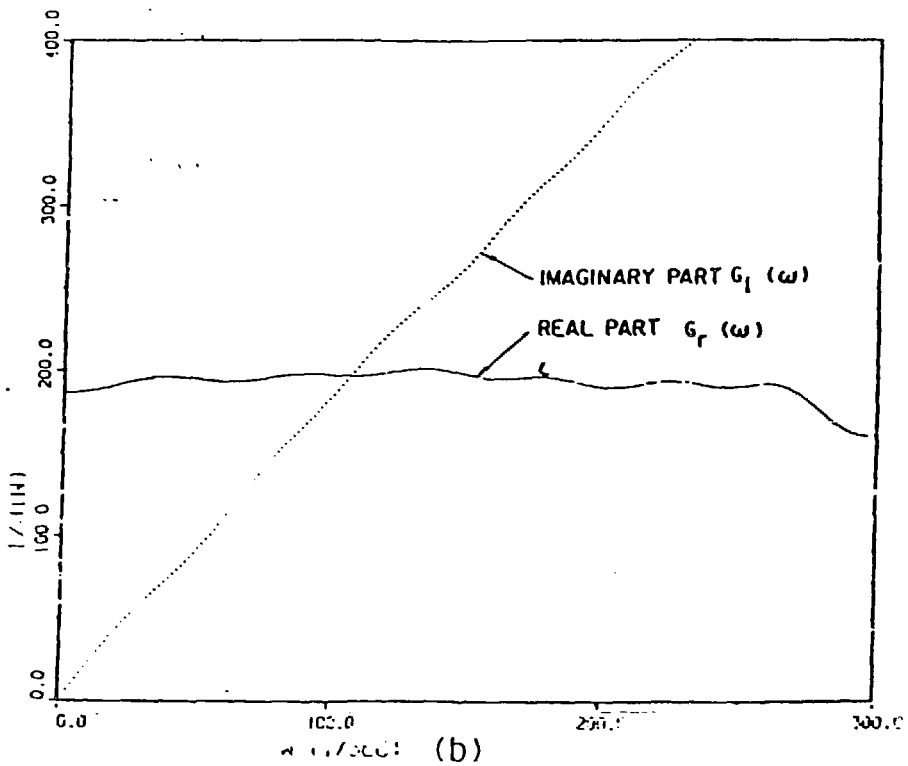


Fig. 14.

(a) Transfer function H(ω) at x = 15 cm for the medium 40 cm cylinder, as a function of ω. Dotted line is calculated from FELIX data, and the two solid lines are one pole and two pole representations. One pole fit becomes worse for small ω.

(b) Reciprocal of the transfer function at same condition. Real part and imaginary part are no longer constant and linear, respectively.

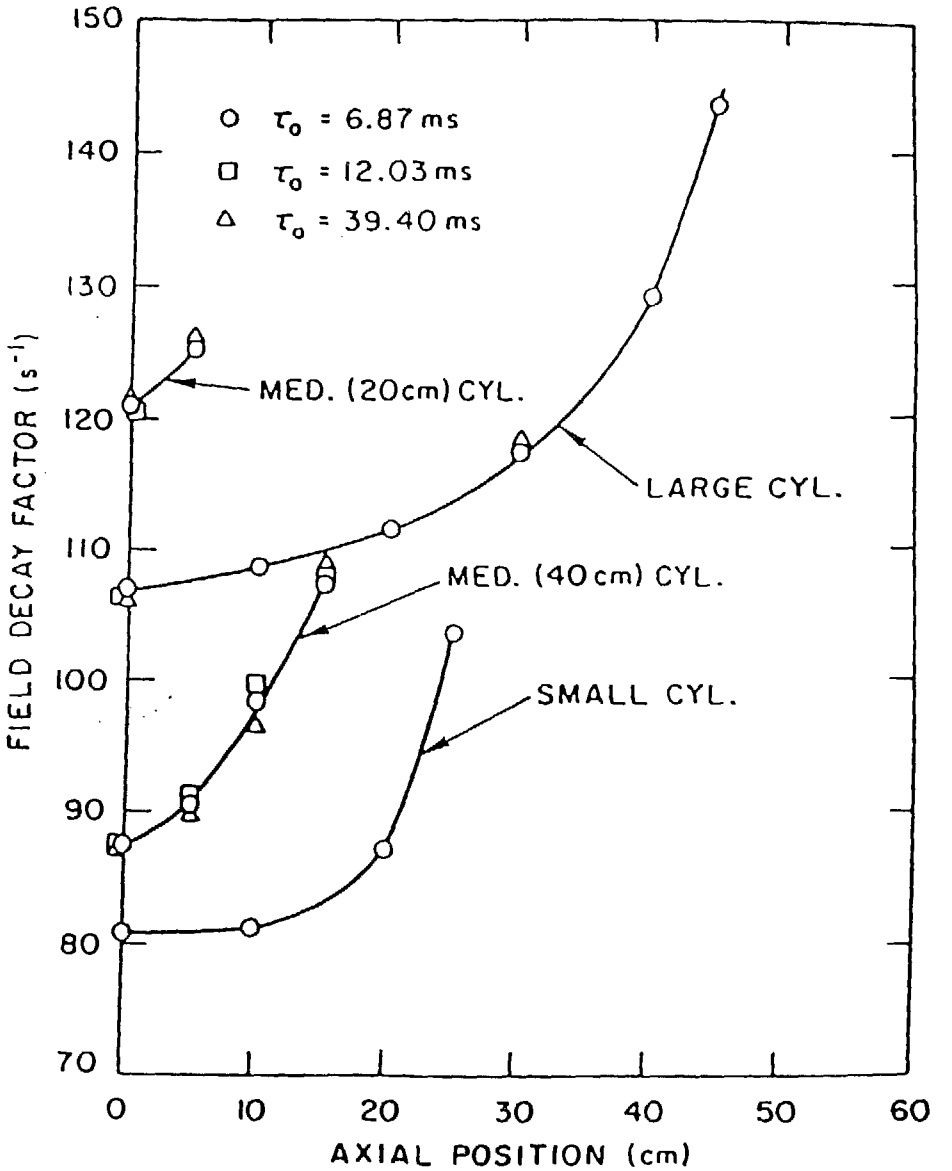


Fig. 15. Field decay factor of the impulse response at different axial positions within the four cylinders. Points with 6.87ms dipole time constant are connected by lines.

function of pole position, where $H(\omega)$ and $\bar{H}(\omega)$ are actual and fitted transfer functions, respectively. That behavior indicates very good selectivity of the poles using this transfer function analysis.

Table 6

TRANSFER FUNCTIONS FOR LARGE CYLINDER

$\gamma_o = 145.56\ s^{-1}$

| Axial Position (cm) | | Pole 1 $\gamma_1$ ($s^{-1}$) | Pole 1 $C_1$ ($s^{-1}$) | Pole 2 $\gamma_2$ ($s^{-1}$) | Pole 2 $C_2$ ($s^{-1}$) | SSDR* ($\times 10^{-3}$) | $\Delta t_o$ (ms) |
|---|---|---|---|---|---|---|---|
| 0 | 1 pole fit | 107.2 | 0.971 | - | - | 0.291 | -0.48 |
| | 2 pole fit | 107.1 | 0.962 | 16.3 | $0.48 \times 10^{-2}$ | 0.188 | |
| 10 | 1 pole fit | 108.0 | 0.956 | - | - | 0.175 | |
| | 2 pole fit | 108.7 | 0.953 | 20.6 | $0.34 \times 10^{-2}$ | 0.138 | |
| 20 | 1 pole fit | 111.4 | 0.927 | - | - | 0.203 | |
| | 2 pole fit | 111.4 | 0.921 | 15.0 | $0.32 \times 10^{-2}$ | 0.136 | |
| 30 | 1 pole fit | 118.1 | 0.856 | - | - | 0.217 | -0.51 |
| | 2 pole fit | 117.3 | 0.852 | 7.2 | $0.25 \times 10^{-3}$ | 0.212 | |
| 40 | 1 pole fit | 125.4 | 0.713 | - | - | 0.498 | |
| | 2 pole fit | 129.0 | 0.714 | 18.1 | $0.52 \times 10^{-2}$ | 0.330 | |
| 45 | 1 pole fit | 134.1 | 0.594 | - | - | 0.430 | |
| | 2 pole fit | 143.4 | 0.600 | 26.5 | $0.11 \times 10^{-1}$ | 0.488 | |
| 50 | 1 pole fit | 139.8 | 0.484 | - | - | 1.010 | |
| | 2 pole fit | 151.9 | 0.491 | 22.8 | $0.80 \times 10^{-2}$ | 0.886 | |

* SSDR (Sum of Squared Deviation Ratio) = $\Sigma\ (H - \overline{H})^2 / \Sigma\ H^2$

Table 7

TRANSFER FUNCTIONS FOR MEDIUM 40 cm CYLINDER

$\gamma_0 = 145.56\ s^{-1}$

| Axial Position (cm) | | Pole 1 $\gamma_1$ ($s^{-1}$) | Pole 1 $C_1$ ($s^{-1}$) | Pole 2 $\gamma_2$ ($s^{-1}$) | Pole 2 $C_2$ ($s^{-1}$) | SSDR* ($\times 10^{-3}$) | $\Delta t_o$ (ms) |
|---|---|---|---|---|---|---|---|
| 0 | 1 pole fit | 88.4 | 0.986 | - | - | 0.094 | -0.80 |
| | 2 pole fit | 87.7 | 0.980 | 9.4 | $0.54 \times 10^{-3}$ | 0.107 | |
| 5 | 1 pole fit | 90.6 | 0.929 | - | - | 0.190 | -0.34 |
| | 2 pole fit | 90.7 | 0.923 | 15.3 | $0.30 \times 10^{-2}$ | 0.152 | |
| 10 | 1 pole fit | 97.4 | 0.805 | - | - | 0.332 | -0.45 |
| | 2 pole fit | 98.6 | 0.799 | 20.5 | $0.58 \times 10^{-2}$ | 0.231 | |
| 15 | 1 pole fit | 106.5 | 0.551 | - | - | 1.114 | -0.69 |
| | 2 pole fit | 107.3 | 0.545 | 14.7 | $0.40 \times 10^{-2}$ | 0.812 | |

* SSDR (Sum of Squared Deviation Ratio) = $\Sigma\ (H - \overline{H})^2 / \Sigma\ H^2$

Table 8

**TRANSFER FUNCTIONS FOR MEDIUM 20 cm CYLINDER**

$\gamma_0 = 145.56\ s^{-1}$

| Axial Position (cm) | | Pole 1 $\gamma_1$ ($s^{-1}$) | Pole 1 $C_1$ ($s^{-1}$) | Pole 2 $\gamma_2$ ($s^{-1}$) | Pole 2 $C_2$ ($s^{-1}$) | SSDR* ($\times 10^{-3}$) | $\Delta t_o$ (ms) |
|---|---|---|---|---|---|---|---|
| 0 | 1 pole fit | 120.6 | 0.804 | - | - | 0.251 | -0.62 |
| | 2 pole fit | 121.0 | 0.800 | 13.9 | $0.30 \times 10^{-2}$ | 0.167 | |
| 5 | 1 pole fit | 125.4 | 0.618 | - | - | 0.305 | -0.62 |
| | 2 pole fit | 125.2 | 0.615 | 13.5 | $0.16 \times 10^{-2}$ | 0.248 | |

* SSDR (Sum of Squared Deviation Ratio) = $\Sigma\ (H - \bar{H})^2 / \Sigma\ H^2$

Table 9

TRANSFER FUNCTIONS FOR SMALL CYLINDER

$\gamma_0 = 145.56\ s^{-1}$

| Axial Position (cm) | | Pole 1 $\gamma_1$ ($s^{-1}$) | Pole 1 $C_1$ ($s^{-1}$) | Pole 2 $\gamma_2$ ($s^{-1}$) | Pole 2 $C_2$ ($s^{-1}$) | SSDR* ($\times 10^{-3}$) | $\Delta t_0$ (ms) |
|---|---|---|---|---|---|---|---|
| 0 | 1 pole fit | 80.4 | 1.065 | - | - | 0.204 | |
| | 2 pole fit | 80.9 | 1.094 | 14.6 | $0.33 \times 10^{-2}$ | 0.186 | |
| 10 | 1 pole fit | 80.8 | 1.122 | - | - | 0.232 | |
| | 2 pole fit | 81.1 | 1.112 | 18.7 | $0.09 \times 10^{-2}$ | 0.126 | |
| 20 | 1 pole fit | 86.7 | 1.084 | - | - | 0.156 | -0.72 |
| | 2 pole fit | 87.2 | 1.079 | 18.4 | $0.58 \times 10^{-2}$ | 0.112 | |
| 25 | 1 pole fit | 101.9 | 0.931 | - | - | 0.453 | -0.74 |
| | 2 pole fit | 103.7 | 0.917 | 29.6 | $0.13 \times 10^{-1}$ | 0.324 | |

*SSDR (Sum of Squared Deviation Ratio) = $\Sigma\ (H - \overline{H})^2 / \Sigma\ H^2$

## 5. Discussion

Results of the one- and two-pole transfer function analysis and the two and three exponential fitting for the induced field from the cylinders are in agreeement. In particular:

1) The one-pole transfer function and two exponential expression fit the data well, but only if the parameters are permitted to change with axial position.

2) The two-pole transfer function and three exponential expression do not give much better fits. Here too a good fit requires that the parameters change with axial position.

Figure 15 shows the striking result that the pole location for the one-pole transfer function varies with axial position but not with the dipole field decay time. Figure 9 shows that large changes in $\gamma_1$ and $\gamma_2$ along the

minimum line for the two exponential expression increase the SSD only slightly. Nevertheless, Table 5 shows that for the best four-parameter fit, both $\gamma_1$ and $\gamma_2$ change with axial position, and neither $\gamma_1$ nor $\gamma_2$ are near $\gamma_0$ = 0.14556 $ms^{-1}$.

A three-parameter $(\gamma_1, C_1, C_2)$ fit was also tried, with $\gamma_2$ = 0.14556 $ms^{-1}$. Table 10 compares the four-parameter fit, the three-parameter fit, and the pole position for the one-pole fit. The value of $\gamma_1$ in the three-parameter fit agrees well with the pole position. The SSD for the three-parameter fit exceeds that for the four-parameter fits by about 0.2 to 0.4 $mT^2$, a value comparable to the large contour on Fig. 9 and ten to twenty times larger than the difference between the best two-exponential fit and the best three-exponential fits in comparable cases.

Figure 16 shows the three-parameter and four-parameter fits to the induced field at the 0 cm and 30 cm positions. Differences between the curves are just discernable. If the induced field data really represents the combined effects of many current modes, then perhaps it is not surprising that a three-parameter fit to two exponentials fits the data well, but a four-parameter fit fits it better.

Table 10

**COMPARISON OF TWO-EXPONENTIAL AND ONE-POLE ANALYSES FOR THE LONG CYLINDER, 6.87 ms time CONSTANT**

| Position | cm | 0 | 10 | 20 | 30 | 40 | 45 |
|---|---|---|---|---|---|---|---|
| | | **Four-Parameter Fit** | | | | | |
| $\gamma_1$ | $ms^{-1}$ | 0.0959 | 0.0967 | 0.0993 | 0.1016 | 0.1005 | 0.1005 |
| $\gamma_2$ | $ms^{-1}$ | 0.1706 | 0.1669 | 0.1689 | 0.1733 | 0.1972 | 0.2077 |
| SSD | $mT^2$ | 1.237 | 1.558 | 1.492 | 0.725 | 1.105 | 1.942 |
| | | **Three-Parameter Fit: $\gamma_2$ = 0.14556 $ms^{-1}$** | | | | | |
| $\gamma_1$ | $ms^{-1}$ | 0.1065 | 0.1059 | 0.1100 | 0.1147 | 0.1236 | 0.1300 |
| SSD | $mT^2$ | 1.529 | 1.760 | 1.672 | 0.919 | 1.517 | 2.423 |
| ΔSSD | $mT^2$ | 0.292 | 0.202 | 0.180 | 0.194 | 0.412 | 0.481 |
| | | **One-Pole Fit: $\gamma_0$ = 0.14556 $ms^{-1}$** | | | | | |
| $\gamma$ | $ms^{-1}$ | 0.1072 | 0.10801 | 0.1114 | 0.1181 | 0.1254 | 0.1341 |

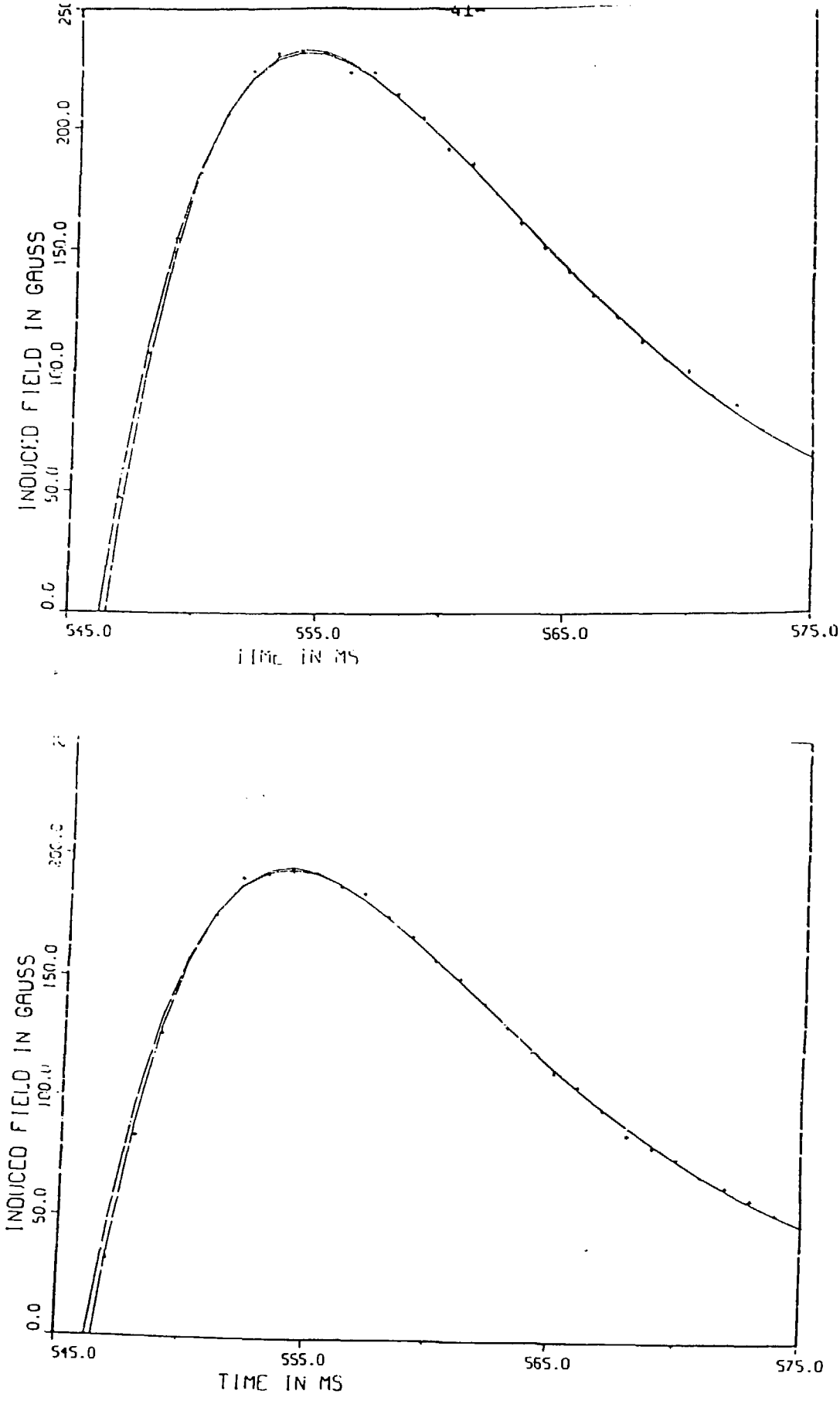


Fig. 16. Three and four parameter fits to the induced field with large cylinder with $\tau$ = 6.87ms. (a) 0 cm axial position, (b) 30 cm axial position.

## 6. Acknowledgment

The authors gratefully acknowledge the assistance of Gary Gunderson, Martin Knott, Alphonso Sistino and Thomas Summers in analyzing the data.

## References

[1] W. F. Praeg, L. R. Turner, J. Biggs, J. Bywater, R. Fuja, M. Knott, R. J. Lari, D. G. McGhee, and R. B. Wehrle, "FELIX, An Experimental Facility to Study Electromagnetic Effects for First Wall, Blanket, and Shield Systems," in Proc. 9th Symp. on Engineering Problems in Fusion Research, IEEE Pub. No. 81CH1715, 1981, pp. 1763-1766.

[2] L. R. Turner, W. F. Praeg, M. J. Knott, R. J. Lari, D. G. McGhee, and R. B. Wehrle, "FELIX Construction Status and Experimental Program," Nucl. Technol./Fusion, Vol. 4, No. 2, Pt. 2, pp. 745-750, 1983.

[3] D. W. Weissenburger, J. M. Bialek, G. J. Cargulia, M. Ulrickson, M. J, Knott, L. R. Turner, and R. B. Wehrle, "Experimental Observations of the Coupling between Induced Currents and Mechanical Motion in Torsionally Supported Square Loops and Plates," to be published.

[4] T. Q. Hua, R. E. Nygren, and L. R. Turner, "Studies of Coupling between Displacement and Eddy Currents in the FELIX Plate Experiment," to be published.

[5] L. R. Turner, G. R. Gunderson, M. J. Knott, D. G. McGhee, W. F. Praeg, and R. B. Wehrle, "Results from the FELIX Experiments on Electromagnetic Effects in Hollow Cylinders," IEEE Transactions on Magnetics, Vol. Mag-21 (1985) pp. 2324-2328.

[6] F. S. Acton, Numerical Methods That Work, New York: Harper and Row, 1970, pp. 252-253.

[7] A. Papoulis, Signal Analysis, New York: McGraw-Hill, 1977, pp. 13-24.